



1

2

3                   **Impact of Multiple Radar Wind Profilers Data**  
4                   **Assimilation on Convective Scale Short-Term Rainfall**  
5                   **Forecasts: OSSE Studies over the Beijing-Tianjin-Hebei**  
6                   **region**

6

7

8

9                   Juan Zhao<sup>1</sup>, Jianping Guo<sup>2\*</sup>, and Xiaohui Zheng<sup>1</sup>

10

11

12                   <sup>1</sup>China Meteorological Administration Training Centre, Beijing, 100081, China

13                   <sup>2</sup>State Key Laboratory of Severe Weather, Chinese Academy of Meteorological Sciences, Beijing,

14                   100081, China

15

16

17

18                   \*Correspondence to: Jianping Guo (jpguo@cma.gov.cn; jpguocams@gmail.com)



19

### Abstract

20 The optimal spatial layout for a radar wind profiler (RWP) network in rainfall forecasting, especially  
21 over complex terrain, remains uncertain. This study explores the benefits of assimilating vertical wind  
22 measurements from various RWP network layouts into convective-scale numerical weather prediction  
23 (NWP) through observing system simulation experiments (OSSEs). Synthetic RWP data were  
24 assimilated into the Weather Research and Forecasting (WRF) model using the National Severe Storms  
25 Laboratory three-dimensional variational data assimilation (DA) system for three southwest (SW)-type  
26 heavy rainfall events in the Beijing-Tianjin-Hebei region. Four types of DA experiments were  
27 conducted and compared: a control experiment (CTL) that assimilates data solely from the operational  
28 RWP network, and three additional experiments incorporating foothill (FH), ridge (RD), and combined  
29 foothill-ridge (FH\_RD) RWP network layouts. A detailed examination of the 21 July 2023 case reveals  
30 that the FH\_RD experiment generally exhibits more skillful storm forecasts in terms of areal coverage,  
31 storm mode, and orientation, benefiting from refined mesoscale wind analysis. Particularly, in the RD  
32 experiment, RWP data assimilation notably reduces wind errors and enhances mesoscale dynamics near  
33 the Taihang Mountains upstream of Beijing, crucial for convective initiation (CI). Aggregated score  
34 metrics across all cases also indicate that both FH and RD experiments offer substantial added value  
35 over the operational network alone. Further sensitivity experiments on vertical resolution and  
36 maximum detection height indicate that the RWP system configuration with the highest detection  
37 height achieves the best performance, while lower detection height degrades forecast quality. These  
38 findings highlight the importance of strategic RWP network placement along the Taihang Mountains'  
39 ridge and foothill for short-term quantitative precipitation forecast in the Beijing-Tianjin-Hebei region.



## 40 **1 Introduction**

41 Radar wind profilers (RWPs) are state-of-art meteorological observation instruments that  
42 provide high vertical and temporal resolution wind profiles, capable of detecting fine-scale atmospheric  
43 dynamic structures throughout the troposphere. Researches have demonstrated the capability of RWP  
44 to observe the evolution of mesoscale cyclonic circulations, shear lines, and low-level jets (LLJs),  
45 which are closely associated with the development of heavy rainfall and convection (Dunn, 1986; Guo  
46 et al., 2023; Liu et al., 2003; Wang et al., 2023; Zhong et al., 1996). The wind observations from RWPs  
47 are expected to improve initial conditions and severe weather forecasts for convective-scale numerical  
48 weather prediction (NWP) through data assimilation (DA). Significant progress has been made in RWP  
49 data assimilation, resulting in wind analysis error reduction and short-term forecast skill enhancement  
50 (Benjamin et al., 2004; Bouttier, 2001; Ishihara et al., 2006; Liu et al., 2022; St-James & Laroche, 2005;  
51 Wang et al., 2022; Zhang et al., 2016). Furthermore, efforts in developing quality control and  
52 observation operator schemes are also critical to ensuring the reliability of the observations and  
53 enhancing assimilation effectiveness (Wang et al., 2020; C. Wang et al., 2023; Zhang et al., 2016;  
54 Zhang et al., 2017).

55 In China, the deployment of a nationwide radar wind profiler network initiated in 2008, over 100  
56 sites are deployed by 2020, primarily using 1290 MHz Doppler radar to monitor the lower and middle  
57 atmosphere (Liu et al., 2020). Currently, the nation-wide profiler network is unevenly distributed: the  
58 spatial concentration of RWP sites over densely populated metropolitan regions, such as the Beijing–  
59 Tianjin–Hebei region, Yangtze River Delta, and Pearl River Delta, are above national average, while  
60 the other regions, especially in west-central China, are lagged behind. Notably, in regions where  
61 observation data is relatively abundant, there is still an issue of uneven spatial distribution of stations,  
62 mainly due to the terrain complexity. Taking the RWP network in the Beijing–Tianjin–Hebei (BTH)  
63 region as an example, seven RWPs are deployed in Beijing within an area of approximately 100 km ×  
64 100 km, while there are only 11 profilers in the whole Hebei province (Wang et al., 2022).

65 Accurate short-term forecasts of heavy rainfall are crucial for mitigating the risks posed by  
66 severe weather events in the BTH region, one of China's most densely populated and economically  
67 vital areas. The BTH region includes the cities of Beijing and Tianjin, and the Hebei Province, and is  
68 bounded by the Taihang Mountains to the west and Bohai Bay to the east. Its complex terrain features



69 with high elevations in the northwest and north, gradually transitioning into plain in the south and east.  
70 The dominating weather circulations affecting heavy rainfall in the BTH region include the cold vortex,  
71 the cold trough, and the trough-anticyclone patterns (Sheng et al., 2020; Zhao et al., 2018; Zhou et al.,  
72 2018). The complex underlying surface and the interaction with large- and mesoscale weather  
73 processes make the initiation and maintenance mechanisms of convective systems in BTH region  
74 highly unique. Convective initiation (CI) is especially difficult to predict due to local environmental  
75 uncertainties and the rapid evolution of meteorological variables. The existing RWP network  
76 concentrated in urban and lowland areas, while the mountainous regions like Taihang Mountains,  
77 where significant terrain-induced convection occurs, are in shortage of sufficient wind profile  
78 observation (Liu et al., 2020). These observational gaps can lead to suboptimal initial conditions in  
79 NWP models, thereby reducing the accuracy of short-term precipitation forecasts. Therefore,  
80 optimizing the distribution of RWP network, particularly in Taihang Mountains, could strengthen the  
81 ability to monitor these critical regions and improve quantitative precipitation forecast.

82 Observation System Simulation Experiments (OSSEs) are widely used to assess the impact of  
83 assimilating specific observational data into NWP models (Huang et al., 2022; Zhao et al., 2021a).  
84 Previous studies by Zhang & Pu (2010) and Hu et al. (2017) have demonstrated the effectiveness of  
85 OSSEs in evaluating the benefits of assimilating wind profiler data for improving forecasts. Recent  
86 research (Bucci et al., 2021; Huo et al., 2023) has also highlighted the advantages of joint assimilation  
87 of multiple observational platforms to enhance analysis of convective dynamics, underlining the  
88 importance of an optimized RWP network. These OSSEs have provided valuable insights into the  
89 strategic RWP site placement to maximize their impact on model performance. To our knowledge,  
90 there are few peer-reviewed published research investigating the potential benefits of RWP network  
91 associated with complex terrain on mesoscale and convective scale weather forecasts (Bucci et al., 2021;  
92 Hu et al., 2017; Huo et al., 2023; Zhang and Pu, 2010).

93 To investigate the impact of RWP network associated with complex terrain on heavy rainfall  
94 forecasts, we focus on southwest (SW)-type rainfall events associated with southwesterly flow, which  
95 constitutes approximately 40% of the total circulation patterns in the BTH region during early summer  
96 (Li et al., 2024; Zhou et al., 2018). When warm, moist air from the south meets the cold air from the  
97 Taihang Mountains, the terrain causes the air to rise, enhancing convective activity. Meanwhile, the  
98 topography of the Taihang Mountains affects the distribution and intensity of the wind field, particularly



99 during severe convective weather events. For example, prior study showed that the  
100 quasi-linear convective systems with extreme heavy rainfall primarily occurred at the foothills of the  
101 Taihang Mountains or in the plains close to the foothills (Sheng et al., 2020). To address observational  
102 gaps, simulated RWP stations are strategically placed along the ridge and foothills, reinforcing the  
103 existing operational network.

104 In this study, the following questions will be addressed. How does the assimilation of RWPs from  
105 ridge and foothill sites combined with that from operational stations impact heavy rainfall forecast in the  
106 BTH region? Does ridge and foothill networks offer added forecast skill over operational RWP network  
107 on short-term convective-scale NWP? Are the benefits of assimilating RWP observations sensitive to the  
108 vertical resolution and maximum detection height of profilers? Ultimately, this research aims to  
109 provide guidance on optimizing the RWP network to improve forecasting accuracy for heavy rainfall  
110 events in the BTH region, thereby enhancing disaster preparedness and response strategies in the  
111 region.

112 To address these questions, a series of OSSEs are conducted, assuming a perfect model, using  
113 three representative southwest (SW)-type heavy rainfall cases. The remainder of this paper is organized  
114 as follows: Section 2 provides an overview of NWP model and data assimilation system. Truth and  
115 background simulation configuration, synthetic observations, experiment design, and evaluation  
116 methods are presented in Sect. 3. Section 4 presents the analysis and forecast results for the 21 July  
117 2023 case, as well as the aggregated performance across all three cases. Section 5 summarizes the key  
118 findings and conclusions.

## 119 **2 Model and Data Assimilation System**

120 The forecast model used in this study is the version 3.7.1 of the Weather Research and  
121 Forecasting Model (WRF) with the Advanced Research WRF (ARW) dynamic solver (WRF-ARW;  
122 Skamarock et al., 2008). All DA and forecast experiments are performed on a 1.5-km space grid of  
123 408×480 horizontal points and 51 vertical levels with a model top at 50-hPa. The domain is centered in  
124 the northern part of China covering the Beijing–Tianjin–Hebei region. The physical parameterizations  
125 include the National Severe Storms Laboratory (NSSL) two-moment four-ice category bulk  
126 microphysics scheme (Mansell et al., 2010; Mansell and Ziegler, 2013; Ziegler, 1985), the Rapid



127 Radiative Transfer Model (RRTM) longwave radiation scheme (Mlawer et al., 1997), the Dudhia  
128 shortwave radiation scheme (Dudhia, 1989), the Rapid Update Cycle (RUC) land surface scheme  
129 (Benjamin et al., 2004), and the Yonsei University (YSU) planetary boundary layer scheme (Hong et  
130 al., 2006).

131 This research employs the NSSL Experimental Warn-on-Forecast (WoF) 3DVAR system  
132 (NSSL3DVAR) (Gao et al., 2013, 2016; Gao & Stensrud, 2014; Wang et al., 2019; Zhuang et al., 2016),  
133 specifically designed for convective-scale Numerical Weather Prediction (NWP) and thunderstorm  
134 forecasting (Gao et al., 2024; Heinselman et al., 2024). The NSSL3DVAR system assimilates  
135 multi-sensor high-resolution observations like radar radial velocity and reflectivity, satellite-retrieved  
136 cloud water path, total precipitable water and atmospheric motion vector, Geostationary Lightning  
137 Mapper (GLM)-derived water vapor, sounding, and surface data (Fierro et al., 2016, 2019; Hu et al.,  
138 2020; Lai et al., 2019; Pan et al., 2018; Zhao et al., 2021b, 2022). To enhance wind field analysis,  
139 particularly in PBL, this study incorporates a RWP assimilation module into the system. Since heavy  
140 rainfall and other severe weather events require fast and timely delivery of forecasts and early warning  
141 to the public, computationally efficient 3DVAR, is quite suitable for the severe weather forecasts by  
142 providing highly efficient and rapid updating analysis and forecast, such as 15-min cycle intervals. Our  
143 focus is to assess the potential impacts of RWP network on convective-scale analysis and short-term  
144 severe weather prediction with this efficient DA method, so we did not use the ensemble derived  
145 background error covariance, which is also incorporated in the variational framework (Gao et al., 2016;  
146 Gao & Stensrud, 2014; Wang et al., 2019).

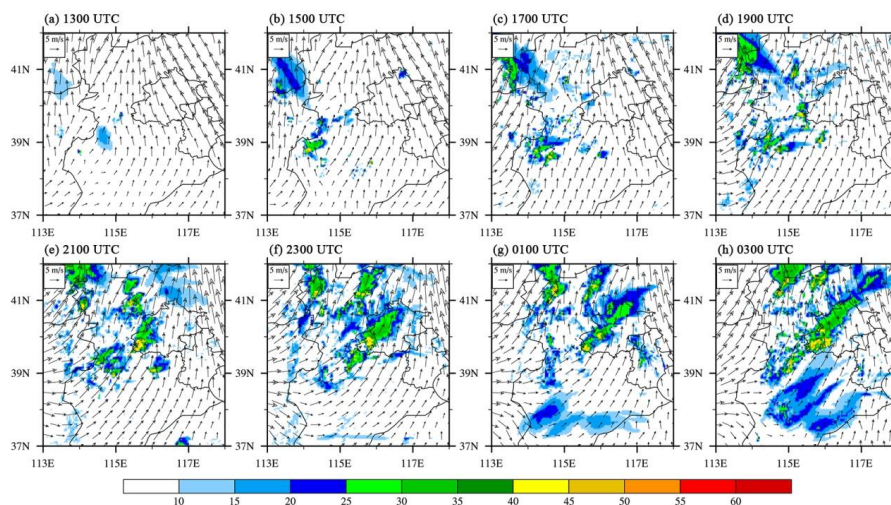
### 147 **3. Experimental design**

#### 148 **3.1 Truth run and background run for OSSE**

149 In the OSSE, synthetic RWP observations are generated by adding observation errors to the truth  
150 run. To obtain this truth run, the WRF model is initialized with the fifth-generation European Centre  
151 for Medium-range Weather Forecasts (ECMWF) atmospheric reanalysis of the global climate (ERA5;  
152 Hersbach et al., 2020; Hoffmann et al., 2019), based on the model configuration and parameterization  
153 schemes described in Sect. 2. Three SW-type heavy rainfall cases that occurred over the  
154 Beijing-Tianjin-Hebei region on 28 June, 12 July, and 21 July of 2023 are selected to construct OSSEs



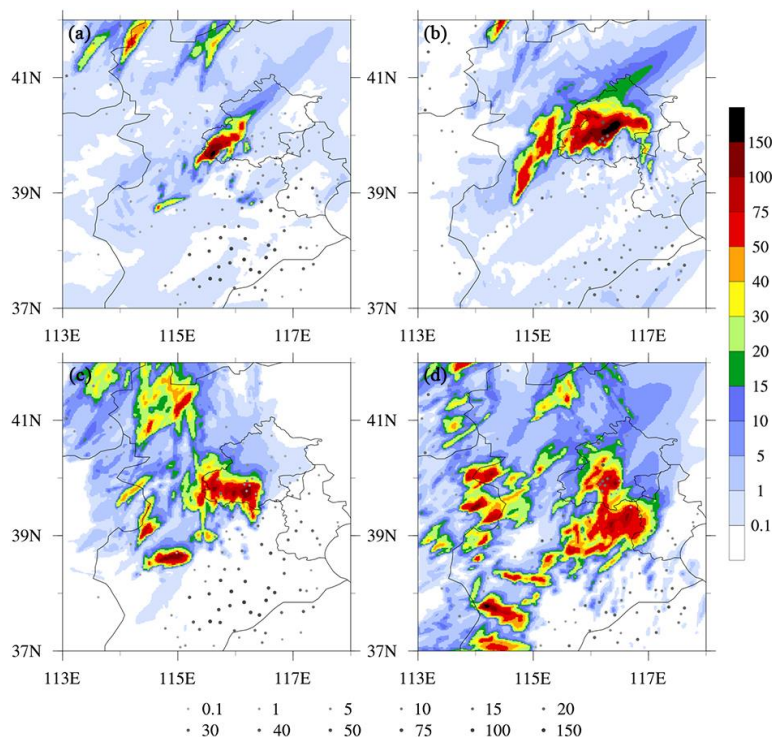
155 and assess the impact of RWP data observed from different spatial layout schemes on convective  
156 initiation and the development of storms. For each case, the truth run is cold started from the start of  
157 DA cycling and integrated for 15 hours, with the boundary conditions also provided by the hourly  
158 ERA5 data. An overview of composite reflectivity in the truth simulation from the case on 21 July  
159 2023 is shown in Fig. 1 as an example. This case was characterized by the presence of an upper-level  
160 trough gradually moving eastward into the Beijing-Tianjin-Hebei region, accompanied by a  
161 corresponding low-level vortex before the evening of 20 July. Meanwhile, southeasterly winds at the  
162 lower levels continuously transported moisture, leading to high instability in central Hebei, and in the  
163 western and southern parts of Beijing. The combination of easterly winds and topographical effects  
164 created favorable conditions for heavy precipitation. Several discrete storms initiated and developed in  
165 west-central Hebei near the foothills of the Taihang Mountains (Fig. 1a-c). With the westerly trough  
166 moving east and strong southerly airflow strengthening water vapor transport, scattered convective  
167 cells formed in the vicinity of the boundary between Hebei and southwestern Beijing around 1900 UTC  
168 on 20 July, then aggregated and developed into a mesoscale convective system in southwest of Beijing  
169 (Fig. 1d-f). Additionally, convective storms in west-central Hebei gradually moved northeastward and  
170 merged with the mesoscale convective system (Fig. 1g). The convective system slowly moved  
171 northeastward and elongated in the southwest–northeast direction (Fig. 1h), persisting across  
172 west-central Beijing until 0900 UTC on 21 July 2023 (Fig. 2).



173  
174 **Figure 1.** Simulated composite reflectivity (dBZ, shaded) and winds at 700 hPa ( $\text{m s}^{-1}$ , vectors) for the  
175 truth simulation from 1300 UTC 20 July to 0300 UTC 21 July, 2023.



176 To prevent unrealistic assumptions about observational capabilities and overly optimistic OSSE  
177 results, the first-guess background run (NoDA) uses the National Centers for Environmental Prediction  
178 (NCEP) Global Forecast System (GFS) forecasts for initial and boundary conditions, which differ from  
179 those of the truth run. The 6-h accumulated precipitation (APCP) forecasts from the truth and  
180 background runs are verified against the rain gauge measurements at national weather stations in the  
181 Beijing-Tianjin-Hebei region (Fig. 2). Compared with the rainfall observations (dots in Fig. 2), the  
182 truth simulation captured the southwest-to-northeast orientation and northeastward movement of the  
183 observed precipitation in Beijing, although it underpredicted the precipitation in southeastern Hebei  
184 (Fig. 2a and b). Conversely, NoDA produced a more west-east oriented rainfall pattern south of Beijing,  
185 rather than a southwest-to-northeast band structure. NoDA missed the precipitation in southeastern  
186 Hebei (Fig. 2c), whereas it overpredicted the rainfall in western Hebei and areas along Beijing's  
187 southern border (Fig. 2d). Notably, the NoDA experiment failed to predict the convection in  
188 southwestern Beijing during the CI stage (discussed later in Sect. 4.1.2).



189  
190 **Figure 2.** The 6-h accumulated precipitation (APCP) forecasts (mm, shaded) from 2100 UTC 20 July  
191 to 0300 UTC 21 July (left), and from 0300 UTC 21 July to 0900 UTC 21 July, 2023 (right) for (a)-(b)





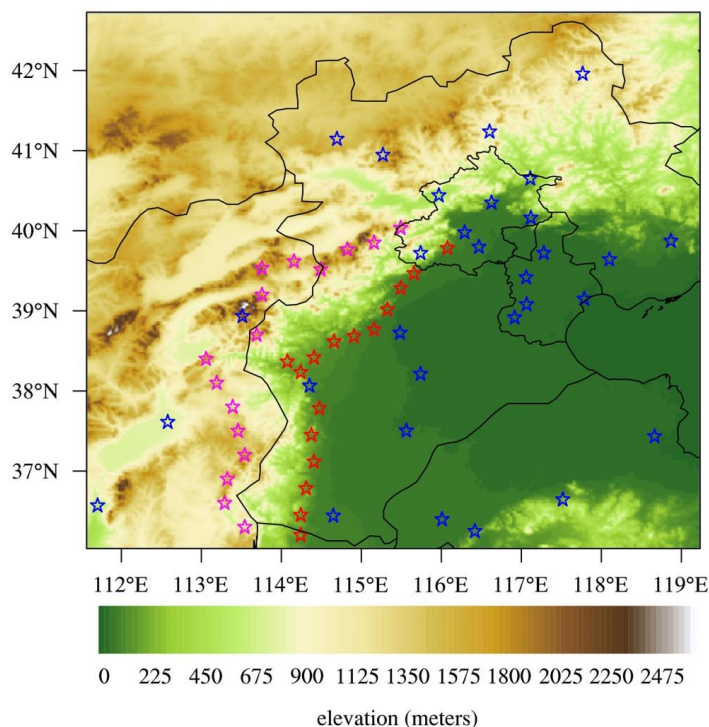
192 Truth, and (c)-(d) NoDA experiments. The dots represent the rain gauge measurements at national  
193 weather stations.

### 194 3.2 Synthetic RWP observations

195 The real-time Chinese RWP network provides horizontal wind direction, horizontal wind speed,  
196 and vertical wind speed at 60-240 m intervals, from the ground surface up to 3-10 km, depending on  
197 the operating frequency (Liu et al., 2020). The network comprises three RWP types: high-troposphere,  
198 low-troposphere, and boundary layer RWPs, with the majority being boundary layer RWPs operating in  
199 the L band. The China Meteorological Administration's data center provides wind profile products at 6-,  
200 30-, and 60-min intervals for each operational site. To generate synthetic profiles of zonal and  
201 meridional wind components ( $u$  and  $v$ ) at operational RWP sites within the simulation domain (30 sites  
202 total), truth wind vectors from model grids are interpolated onto each site using the bilinear  
203 interpolation method (Fig. 3, blue stars). Additionally, we assume more observations are available at  
204 upstream sites near Beijing, specifically along the foothill and ridge of Taihang Mountains (Fig. 3, red  
205 and magenta stars). The spatial locations for the foothill and ridge sites, with a total of 16 sites each, are  
206 determined based on the 1' topographic dataset  
207 ([http://www.ngdc.noaa.gov/mgg/global/relief/ETOPO1/data/bedrock/cell\\_registered/netcdf/](http://www.ngdc.noaa.gov/mgg/global/relief/ETOPO1/data/bedrock/cell_registered/netcdf/)). In this  
208 study, maximum detection heights of 3, 8, and 12 km, and vertical resolutions of 60 and 120 m have  
209 been chosen to mimic the vertical range and resolution of most real RWP data. Synthetic wind profile  
210 at each simulated RWP site is assumed to be at the height  $H$ , which is defined as follows:

$$\begin{aligned} H(1) &= H_{\text{elev}} + 500 \\ H(k) &= H(1) + k \times H_{\text{inc}}, \quad \text{if } H(k) \leq H_{\text{max}} \end{aligned} \quad (1)$$

212 where  $H_{\text{elev}}$  is the elevation of the observation site,  $k$  is the index number of the vertical level,  $H_{\text{inc}}$  and  
213  $H_{\text{max}}$  are specified vertical resolution and maximum detection height, respectively. The units of all  
214 height variables are meters. Similar to Zhang et al. (2016), 500 m is selected as the first level of wind  
215 profile used for assimilation. The final observations are obtained by adding perturbations to the wind  
216 profiles extracted from the truth run. The perturbations are assumed to be normally distributed  
217 Gaussian random errors with a mean of zero and a standard deviation of 2 m/s (Hu et al., 2017; Huang  
218 et al., 2020; Zhao et al., 2021a)..



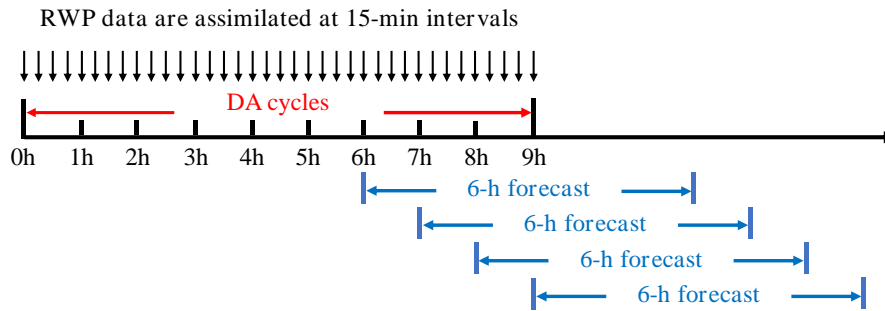
219  
220 **Figure 3.** Spatial distribution of operational RWP network (blue stars), and simulated RWP network  
221 along the foothill (red stars) and ridge (magenta stars) of Taihang Mountains within the simulation  
222 domain, in which the terrain is indicated by color shading.

### 223 3.3 Experimental Design

224 To mimic real-world operations, this OSSE study employs a DA and forecast cycle workflow  
225 similar to the Warn-on-Forecast System (WoFS) real-time Spring Forecast Experiment (SFE) runs  
226 (Heinselmann et al., 2024; Hu et al., 2020; Jones et al., 2018) (Fig. 4). To minimize data contamination  
227 from precipitation, DA cycles are performed before widespread rainfall occurs in the simulation  
228 domain, as wind profile accuracy from RWPs can be degraded by falling hydrometeors (Zhang et al.,  
229 2017). The model initial and boundary conditions for all DA and forecast experiments are derived from  
230 the GFS forecasts. The RWP DA cycles run for 9 hours at 15-min intervals, with a 6-h free forecast  
231 launched every hour starting from the sixth hour of analysis cycles (Fig. 4). This delayed forecast  
232 initiation allows convective systems to develop, as they are typically not yet initiated or developed  
233 during the initial hours of assimilation cycles. For comparison, a first-guess background run (NoDA) is



234 conducted by advancing the model forward without assimilating any observations.



235

236 **Figure 4.** Illustration of the data assimilation and forecast cycle workflow. A 6-h forecast is launched  
 237 every hour from the sixth hour to the end of DA cycles (namely, four separate forecasts).

238 To investigate the impact of simulated foothill and ridge RWP networks on convective-scale  
 239 NWP, four types of DA experiments are performed (Table 1). These experiments differ in their  
 240 assimilation of synthetic profiler data from various RWP network spatial layouts. The baseline  
 241 experiment, CTL, assimilates synthetic observations from the operational RWP network with a vertical  
 242 resolution of 60 m (from 500 m to 8 km height), serving as a benchmark for comparison. This vertical  
 243 resolution represents a best-case scenario for RWP capabilities.

244 **Table 1.** List of the DA sensitivity experiments based on various spatial layout schemes of radar wind  
 245 profiler (RWP) network over the Beijing-Tianjin-Hebei region.

Experiment	Operational	Foothill	Ridge	Maximum height (km)	Vertical resolution (m)
CTL	✓			8	60
FH	✓	✓		8	60
RD	✓		✓	8	60
FH_RD	✓	✓	✓	8	60
FH_RD_V120	✓	✓	✓	8	120
FH_RD_H3	✓	✓	✓	3	60
FH_RD_H12	✓	✓	✓	12	60

246 CTL: control DA experiment; FH: foothill; RD: ridge

247 The second and third types of experiments assimilate the simulated foothill and ridge RWPs,  
 248 respectively, in conjunction with data from operational sites (referred to as FH and RD). The fourth type



249 of experiment FH\_RD is performed by assimilating the operational, foothill, and ridge profilers with the  
250 same vertical resolution and maximum detection height as before. Additionally, three sensitivity  
251 experiments FH\_RD\_V120, FH\_RD\_H3, FH\_RD\_H12 are designed to assess the influence of  
252 assimilating RWP data with different vertical resolution (120 m) and maximum detection heights (3 km,  
253 12 km) on the analyses and forecasts, to address the potential usage of real-time data from RWPs  
254 operating at different frequencies.

255 In all DA experiments, the background errors for zonal and meridional wind components are  
256 specified as 3–6 m/s from the surface to 20 km above ground level (AGL). The observation error is set  
257 to 3 m/s, based on sensitivity tests within the 2–6 m/s range and consistent with previous studies (Hu et  
258 al., 2017; Huo et al., 2023; Wang et al., 2022; Zhang et al., 2016). In the minimization process two  
259 outer loops are adopted, each with a prescribed horizontal and vertical correlation scale for the  
260 recursive filter used in the program (Gao et al., 2004; Purser et al., 2003). Following previous studies  
261 (Wang et al., 2022; Zhao et al., 2022), the horizontal correlation scale lengths are set to be 50 km in the  
262 first loop and 20 km in the second loop. And the corresponding vertical correlation lengths are 5 and 2  
263 grid points, respectively.

### 264 **3.4 Evaluation metrics**

265 This study examines the impact of RWP DA on wind analyses and forecasts during a southwest  
266 (SW)-type heavy rainfall event on 21 July 2023. To obtain an overall insight into the impact of RWP  
267 DA on wind analyses and forecasts, time series and probability density distributions, as well as vertical  
268 profiles of root-mean-square errors (RMSEs) for wind components during the DA cycles and 6-h free  
269 forecasts are calculated for each type of assimilation experiments. Additionally, subjective diagnostic  
270 analyses of wind vectors improved by assimilation of RWPs are also discussed in more detail. To  
271 investigate the impact on short-term forecasts, both qualitative and quantitative assessments of radar  
272 reflectivity and accumulated precipitation forecasts are conducted against the truth run. To evaluate the  
273 performance quantitatively, the neighborhood-based equitable threat score (ETS, Clark et al., 2010) is  
274 calculated using neighborhood radius of 12-km for different thresholds of composite reflectivity (CREF)  
275 and hourly precipitation (HPRCP). Using the same neighborhood radius and thresholds,  
276 contingency-table based metrics including the probability of detection (POD), false alarm ratio (FAR),  
277 success ratio (SR), frequency bias (BIAS), and critical success index (CSI) are also calculated to



278 quantify the CREF and HPRCP forecasts. To account for case-to-case variability, two additional  
279 SW-type heavy rainfall events (28 June and 12 July 2023) are examined. Finally, score metrics are  
280 aggregated from each initialization hour (sixth hour to end of DA cycles) across three cases, ensuring a  
281 fair and consistent measure of forecast skill.

## 282 **4 Results and discussion**

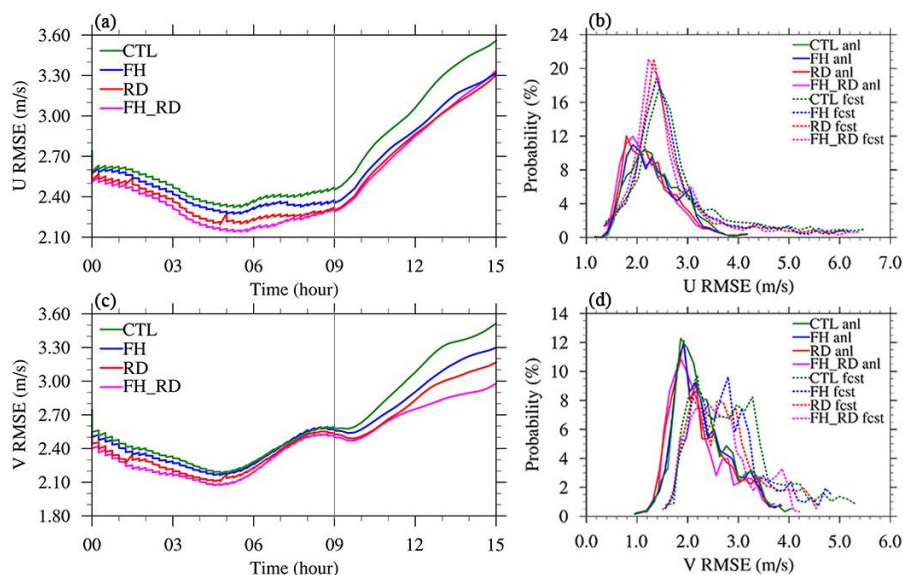
### 283 **4.1 21 July 2023 case**

#### 284 **4.1.1 The impact on wind fields**

285         The first question we attempt to answer is how the spatial distribution of RWP sites should be  
286 planned to optimize the accuracy of short-range convection-resolving NWP system. The influence of  
287 assimilating RWP data from different networks, as described in Sect. 3.3, on wind analysis and forecast  
288 can be straightforwardly assessed by examining the RMSEs of wind components during the 9-h  
289 assimilation cycles and 6-h free forecasts. For clarity, the time series and probability density  
290 distribution (PDF) of the wind RMSEs from the CTL, FH, RD, and FH\_RD experiments are compared  
291 in Fig. 5. The statistics are computed against the truth run at all model levels within the simulation  
292 domain shown in Fig. 3. Overall, the RMSEs of wind analyses from all DA experiments during the  
293 analysis cycling decrease over the first six hours and then gradually increase afterward, exhibiting an  
294 evident staircase pattern (Fig. 5a and c), indicating that the wind field is modified by the NSSL3DVAR  
295 system towards the truth in each analysis cycle. A comparison among all DA experiments reveals that  
296 the FH\_RD experiment yields the smallest wind errors, followed by RD, then FH, with CTL exhibiting  
297 the largest errors. This likely occurs because (a) FH\_RD assimilates the largest amount of wind  
298 observations, while CTL assimilates the fewest, and (b) the uncertainties of wind field in the background  
299 field are larger in mountainous regions than flatlands (this issue will be discussed in detail later in this  
300 section). Although the RMSEs of wind forecasts increase progressively over time, similar trends and



301 behaviors are observed in the 6-h free forecasts, highlighting the impact of wind profile observations  
302 gathered from ridge and foothill networks. It is also noted that the difference in the meridional wind  
303 among FH, RD, and FH\_RD is more pronounced than that of the zonal wind, which can be related to  
304 the varying degree of improvement in the southerly jet intensity. Generally, the PDF figures show that  
305 the distributions of wind analyses are skewed towards smaller error values compared to those of  
306 forecasts, with the wind forecasts exhibiting a heavy tail towards larger error values (Fig. 5b and d).  
307 For example, the analysis errors for the  $v$  variable tend to cluster around 1.6–2.6 m/s, while the PDFs of  
308 forecast errors show peaks near 2.0–3.4 m/s. The patterns in distributions from different assimilation  
309 experiments align with the results observed in the time series analysis.

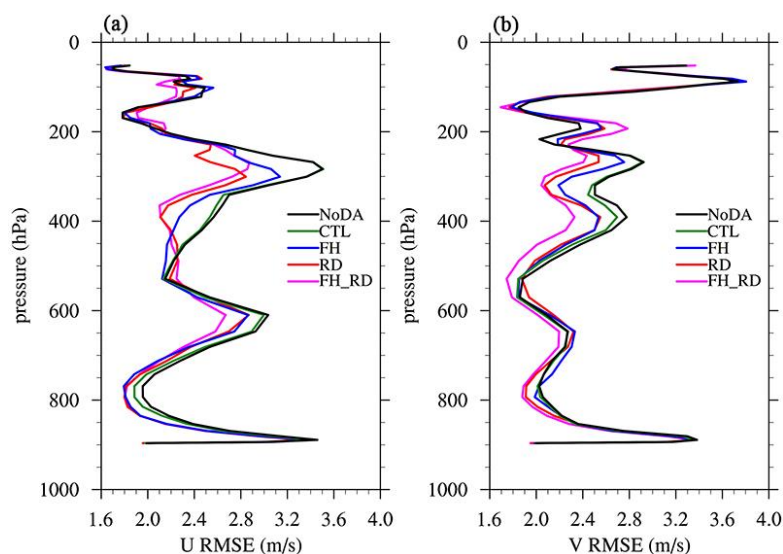


310  
311 **Figure 5.** Time series of root-mean-square errors (RMSEs) for (a)  $u$  ( $\text{m s}^{-1}$ ), and (c)  $v$  ( $\text{m s}^{-1}$ ) analyses  
312 and forecasts from the CTL (green), FH (blue), RD (red), and FH\_RD (magenta) experiments. The thin  
313 grey line separates analysis cycling and 6-h free forecasts. Probability density distribution (PDF) of  
314 RMSEs for (b)  $u$  ( $\text{m s}^{-1}$ ), and (d)  $v$  ( $\text{m s}^{-1}$ ) analyses (dash) and forecasts (dotted) from four experiments.

315 To assess the impact of the DA experiments at different altitudes, Fig. 6 presents the vertical  
316 profiles of domain-averaged RMSEs of wind analyses at the end of the assimilation cycles. Compared



317 to the NoDA experiment, the assimilation of RWPs generally has a positive effect on the wind field  
318 throughout the troposphere. The CTL experiment slightly reduces the wind errors, specifically in the  
319 layer from 850 to 600 hPa for the  $u$  component and from 500 to 300 hPa for both components. It is  
320 clear that the DA experiments assimilating ridge and foothill RWPs outperform CTL, except for the  
321 thin layer between 260 and 160 hPa. For the  $u$  wind component, the RD experiment has a comparable  
322 RMSE profile to FH below 550 hPa but results in a much smaller error above (Fig. 6a). In the analysis  
323 of the  $v$  wind, RD consistently performs better than FH, except for the layer from 260 to 160 hPa (Fig.  
324 6b). Notably, FH\_RD results in the smallest wind errors across most levels, aligning with the  
325 previously observed error trends over time.



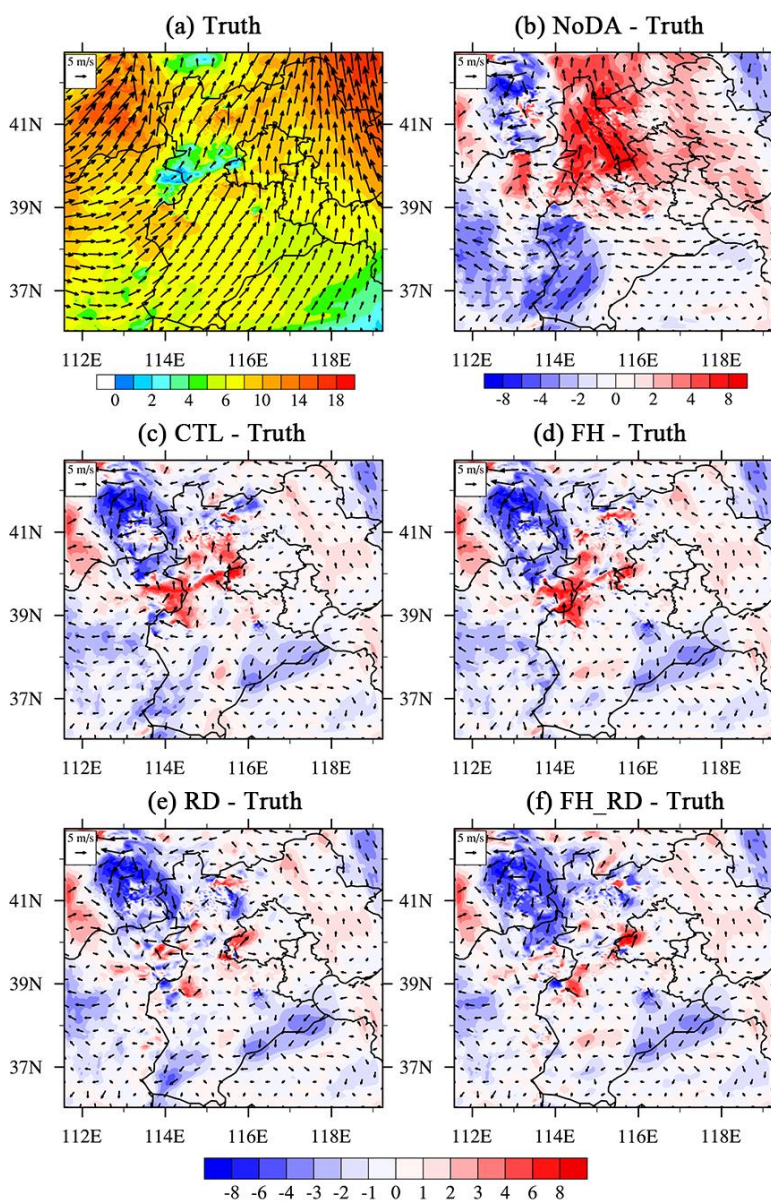
326  
327 **Figure 6.** Vertical profiles of domain-averaged RMSEs for (a)  $u$  ( $\text{m s}^{-1}$ ), and (b)  $v$  ( $\text{m s}^{-1}$ ) analyses at  
328 2100 UTC 20 July 2023 (end of analysis cycling) from the CTL (green), FH (blue), RD (red), and  
329 FH\_RD (magenta) experiments.

330 To examine how the RWP DA adjusts the mesoscale airflow, we present the 700-hPa wind  
331 vectors and wind speeds from all experiments as an illustration of the model's dynamic conditions (Fig.  
332 7). For clarity, Fig. 7b-f compare the differences in wind vectors and wind speeds between the DA  
333 experiments and the corresponding field from the truth run. These differences, considered as wind  
334 errors, help evaluate how assimilating RWPs from different observation networks adjusts the wind field.  
335 The red (blue) color represents positive (negative) wind speed bias compared to the truth. In the NoDA



336 experiment, there is a notable southeasterly wind bias in Beijing and the mountainous regions to its  
337 west, characterized by excessively high wind speeds. Conversely, the true simulation reveals a strong  
338 southwesterly flow (Fig. 7b). Meanwhile, the southwest wind is remarkably weaker in southwestern  
339 Hebei (at the foothills of the Taihang Mountain), and the westerly wind in the upstream Taihang  
340 Mountains region is also underestimated. The CTL experiment significantly reduces the easterly wind  
341 bias in Beijing and its surrounding areas while enhancing the southwesterly winds in Hebei (Fig. 7c).  
342 However, unignorable wind errors persist upstream of Beijing, particularly along the mountainous  
343 regions, due to the absence of operational wind profiler sites. The FH experiment produces wind  
344 adjustments similar to those in CTL but further reduces wind errors in the plains of Hebei by  
345 assimilating observations from foothill sites (Fig. 7d). Conversely, with the assimilation of RWP data  
346 from the ridge network, both RD and FH\_RD significantly reduce positive wind speed errors upstream  
347 of Beijing along the mountains, which is crucial for convection initiation (CI) near the boundary  
348 between Hebei and southwestern Beijing (Fig. 7e and f). While the southwest winds in southwestern  
349 Hebei remain slightly weaker in RD, FH\_RD addresses this by assimilating ridge RWPs alongside  
350 foothill data. However, all DA experiments still show negative wind speed errors and  
351 northwesterly/northeasterly wind direction errors near the border of Shanxi, Hebei, and Inner Mongolia,  
352 with errors even larger than those in NoDA. This is mainly due to the lack of RWP observations in this  
353 tri-provincial border area. As a result, the influence of ridge RWP data may propagate northward into  
354 this region by the RD and FH\_RD experiments, significantly reducing positive errors upstream of  
355 Beijing along the mountains but increasing negative errors in this area.





356

357 **Figure 7.** (a) 700-hPa wind (vectors) with wind speed ( $\text{m s}^{-1}$ , color shaded) from the truth run, and  
358 differences between the 700-hPa winds from (b) NoDA, (c) CTL, (d) RD, (e) FH, and (f) FH\_RD  
359 experiments and the truth run at 2100 UTC 20 July 2023 (end of analysis cycling).

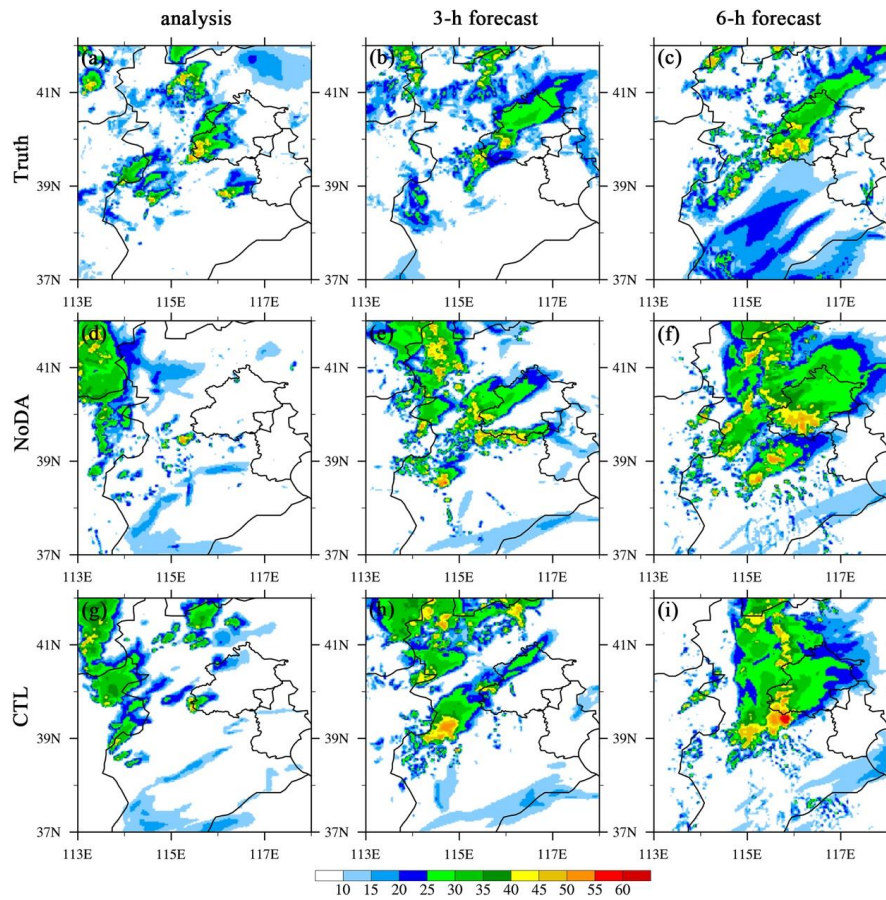
#### 360 4.1.2 The impact on reflectivity and precipitation forecasts

361

The analysis, along with the 3- and 6-h forecasts of composite reflectivity from all experiments,



362 is compared to the truth run in Fig. 8 and 9. In the southwest of Beijing, a convective system initiates  
363 and develops. As it merges with scattered storms originating in western Hebei near the foothills of the  
364 Taihang Mountains, the system intensifies rapidly. Eventually the convection becomes a  
365 southwest-northeast oriented mesoscale system across the western and central parts of Beijing (Fig.  
366 8a-c). At the initial stage, the NoDA experiment underestimates convection in Beijing and Hebei (Fig.  
367 8d), but in the 6-h forecast, NoDA overpredicts the storm coverage and intensity in Beijing and  
368 produces excessive spurious convection in western and northern Hebei (Fig. 8d-f). At analysis time, all  
369 DA experiments show improvement in the location and shape of the convective system in southwestern  
370 Beijing, and FH\_RD produces the strongest reflectivity analysis (Fig. 8g, 9a, 9d, and 9g). This implies  
371 that the assimilation of RWP data can improve CI timing and location by capturing the mesoscale flow  
372 features in the pre-storm environment (Fig. 7). The RWP DA also helps alleviate storm displacement  
373 and intensity errors and suppress spurious cells in subsequent forecasts, owing to a better representation  
374 of the storm environment. Although CTL correctly analyzes the CI near the observed location, its  
375 analysis and 3-h lead-time reflectivity forecast show that the storm intensity in Beijing is still weaker  
376 than the truth simulation, especially over western and central Beijing (Fig. 8g-i). The FH experiment  
377 alleviates the intensity errors, though with a slightly weaker bias; however, spurious echoes to the west  
378 of Beijing remain evident in the 6-h forecast (Fig. 9a-c). With the assimilation of ridge RWP data, the  
379 RD and FH\_RD experiments further strengthen the CI process and improve the storm pattern and  
380 development. A comparison among all experiments reveals that FH\_RD demonstrates overwhelming  
381 superiority over the other three DA experiments in terms of areal coverage, storm mode, and storm  
382 orientation (Fig. 9g-i).

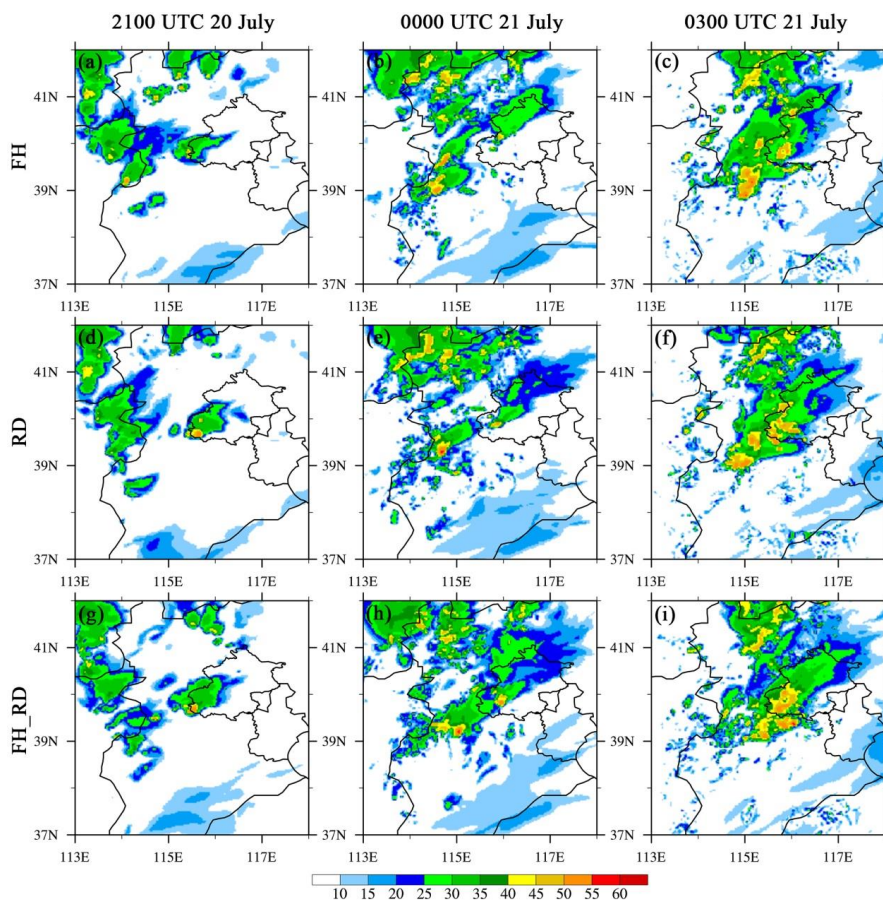


383

384 **Figure 8.** The composite reflectivity (dBZ, shaded) for (left) analysis, (middle) 3-h forecast, and (right)

385 6-h forecast from (a)–(c) truth simulation, (d)–(f) NoDA, and (g)–(i) CTL experiments initialized at

386 2100 UTC 20 July 2023.



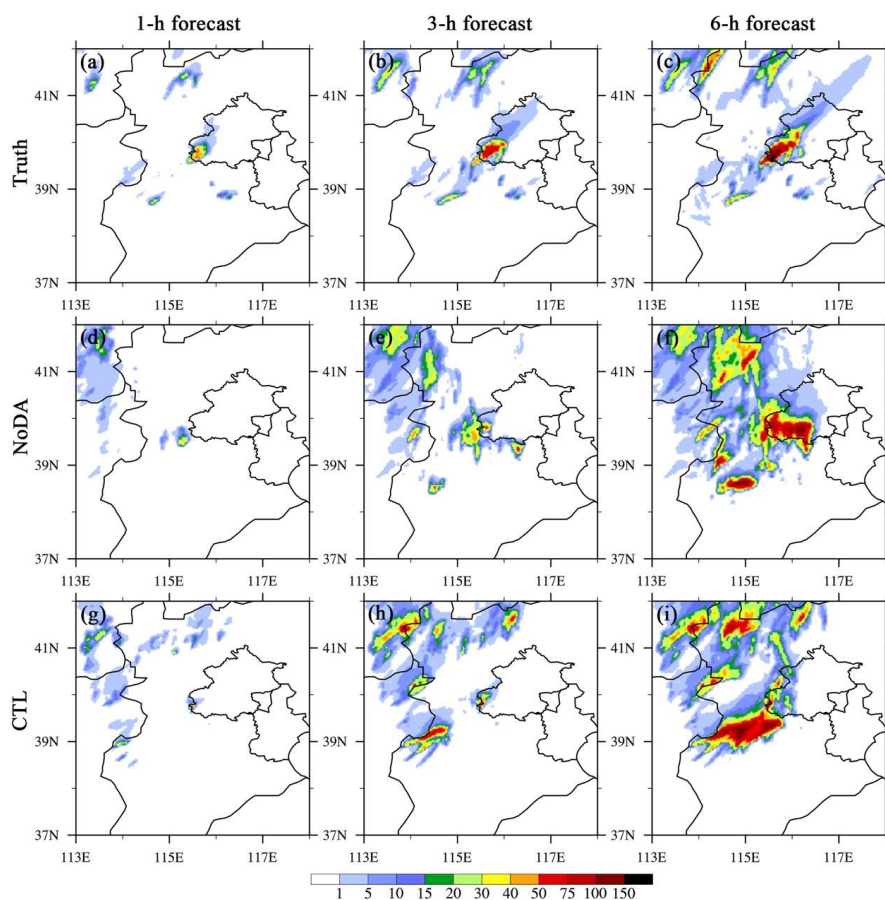
387

388 **Figure 9.** Same as in Fig. 8, but for the composite reflectivity (dBZ, shaded) from (a)–(c) FH, (d)–(f)  
389 RD, and (g)–(i) FH\_RD experiments.

390 Concerning precipitation, the 1-, 3-, and 6-h accumulated precipitation (APCP) forecasts exhibit  
391 similar behavior to the reflectivity results in terms of rainfall location, onset time, and amount (Fig. 10  
392 and 11). As discussed above, all assimilation experiments predict the initial precipitation area and  
393 intensity in the southwest of Beijing more accurately than NoDA, leading to improvements in  
394 subsequent APCP forecasts in this area. For example, assimilating ridge and foothill RWPs corrects the  
395 weaker biases associated with this storm in the 1- and 3-h forecasts (Fig. 11a-b, d-e, g-h). Meanwhile,  
396 the more west-east oriented heavy rainfall occurring over the south of Beijing in the 6-h forecast of  
397 NoDA is revised by the assimilation experiments, shifting to a southwest-northeast orientation that is  
398 closer to the truth simulation. Although the initial areal coverage of rainfall is better captured by CTL  
399 compared to NoDA, CTL still tends to underpredict the precipitation amount in southwestern Beijing,



400 while overestimation is commonly observed in parts of the mountainous areas to the southwest of  
401 Beijing (Fig. 10g-i). One potential factor contributing to the overpredicted rainfall in the mountainous  
402 areas to the southwest of Beijing is the CTL experiment's reduction of positive wind errors in Beijing,  
403 while higher wind speeds (compared to the truth) persist along the upstream mountains. It is due to the  
404 absence of operational wind profiler sites. This creates a favorable environment for heavy rainfall in the  
405 upstream mountain and foothill regions, leading to overestimated rainfall in those areas and  
406 underpredicted precipitation over Beijing. Both RD and FH\_RD experiments yield a smaller areal  
407 coverage of precipitation at the same region, and they also better capture the southwest-northeast  
408 orientation of the rainband in southwestern Beijing (Fig. 11d-i), as the large wind errors in the upstream  
409 mountains are remarkably reduce by assimilating RWP data from the ridge network (Fig. 7e and f). As  
410 expected, the APCP forecasts from FH\_RD align well with the true rainfall estimates in terms of  
411 placement, orientation, and amount (Fig. 11g-i vs. 10a-c).

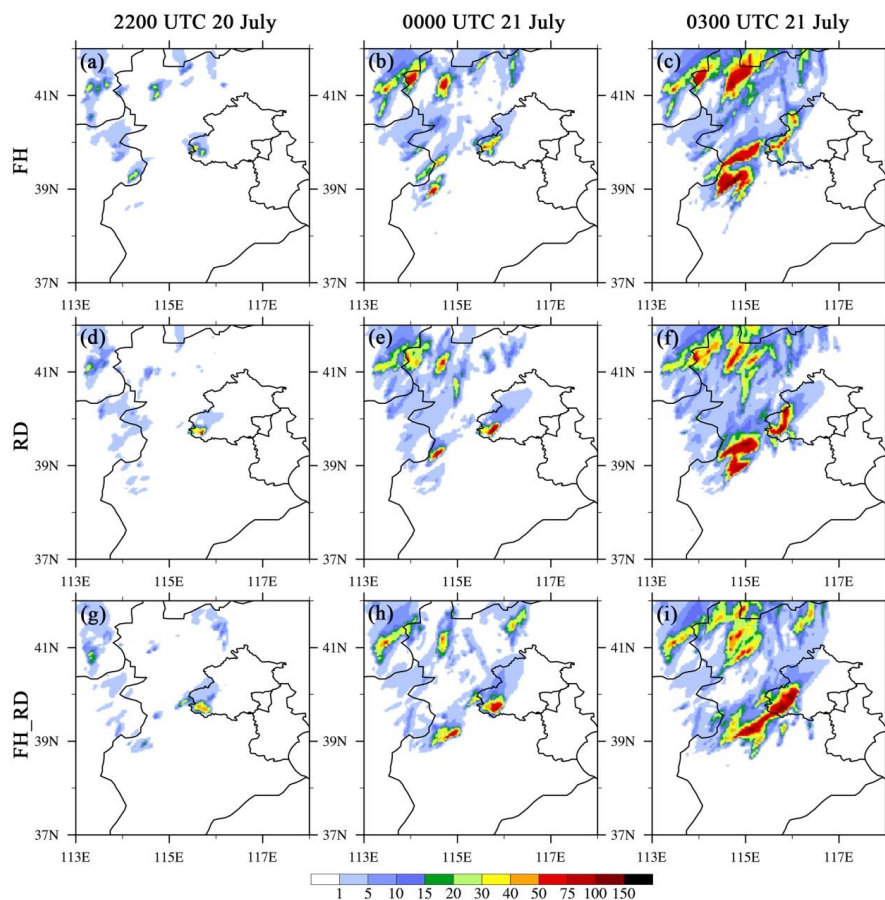


412

413 **Figure 10.** The accumulate precipitation (APCP) forecasts (mm, shaded) for (a)-(c) Truth, (d)-(f)

414 NoDA, and (g)-(i) CTL experiments initialized at 2100 UTC 20 July 2023. The (left) 1-, (middle) 3-,

415 and (right) 6-h forecasts are shown.



416

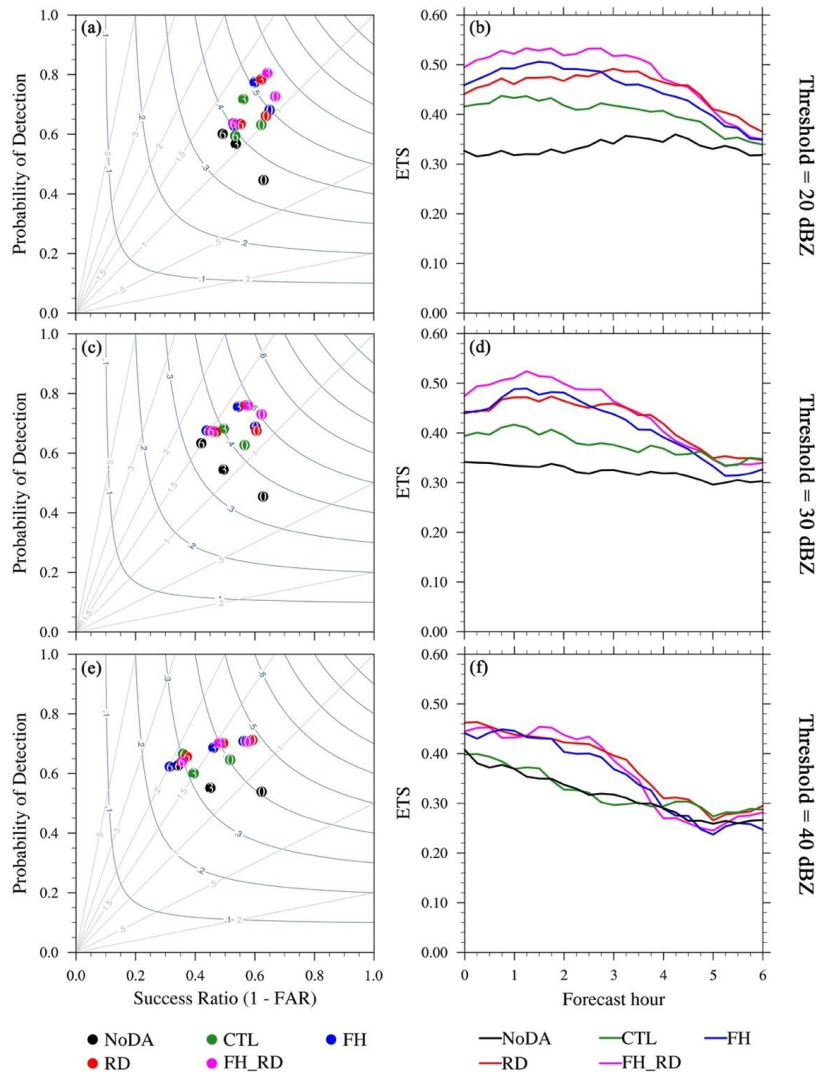
417 **Figure 11.** Same as in Fig. 10, but for the APCP forecasts (mm, shaded) from (a)–(c) FH, (d)–(f) RD,  
418 and (g)–(i) FH\_RD experiments.

419 To quantify the performance of the reflectivity and precipitation forecasts by assimilating RWP  
420 data from different observation networks, categorical performance diagrams and neighborhood-based  
421 ETS are calculated and aggregated over four 6-h free forecasts. These forecasts are launched hourly  
422 from the sixth hour to the end of the analysis cycle. All score metrics are computed for a neighborhood  
423 radius of 12 km. The ETS for composite reflectivity is calculated every 15 minutes, while for APCP, it  
424 is calculated hourly. In the performance diagrams, values of POD, SR (1 – FAR), and CSI closer to  
425 unity indicate higher forecast skill, with the perfect forecast located at the upper-right corner of the  
426 diagram. A BIAS value greater (less) than unity indicates overprediction (underprediction). Because of  
427 decreased PODs along with increased FARs, most experiments show a slight decline in forecast scores  
428 when the composite reflectivity threshold increases from 20 to 40 dBZ (Fig. 12). Overall, all DA



429 experiments consistently outperform NoDA at all thresholds, exhibiting higher POD, SR, CSI, and ETS  
430 values, except for the CTL (FH and FH\_RD) experiment during the 0-4 h (4-5 h) forecast period at the  
431 threshold of 40 dBZ. Among them, the FH\_RD, RD, and FH experiments show overwhelming  
432 superiority over CTL. Upon further comparison, it is evident that FH\_RD produces the highest POD,  
433 SR, CSI, and ETS, as well as the smallest BIAS for the 20- and 30-dBZ thresholds. However, for 40  
434 dBZ, the RD experiment performs slightly better than FH\_RD at most forecast lead times. It is also  
435 worth noting that FH generally produces higher forecast scores than RD does before the 2-h forecast  
436 lead time, while RD exhibits better forecast skill thereafter. This suggests that assimilating RWP data  
437 from the foothill network is more effective in the first two hours, while ridge site observations have a  
438 more pronounced positive impact between 2 and 6 hours. Additionally, the period during which FH  
439 outperforms RD shortens when the threshold increases from 20 to 40 dBZ.

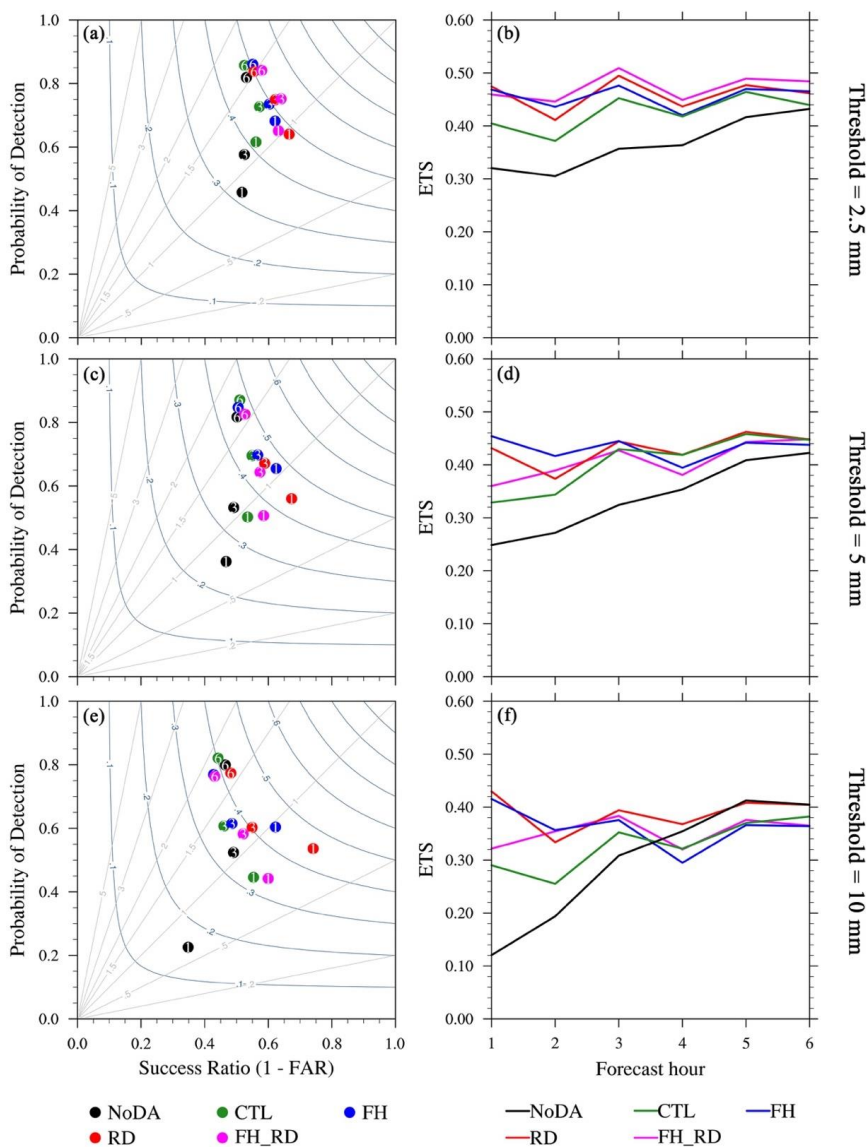




440  
 441 **Figure 12.** Aggregate score metrics of 0-6 h composite reflectivity (CREF) forecasts aggregated from  
 442 each initialization hour from the sixth hour to the end of DA cycles for case 1 for the NoDA (black),  
 443 CTL (green), FH (blue), RD (red), and FH\_RD (magenta) experiments. (left) The performance  
 444 diagrams, and (right) the equitable threat score (ETS) for (a)–(b) 20 dBZ, (c)–(d) 30 dBZ, and (e)–(f)  
 445 40 dBZ thresholds, respectively. Results are shown for a neighborhood radius of 12-km. The numbers  
 446 within the colored dots in the performance diagrams denote the forecast hour (i.e. 0-, 3- and 6-h  
 447 forecasts).



448           A similar trend and behavior are observed in the performance diagrams and ETS figures for the  
449 HPRCP forecast, highlighting the superior performance of the RD and FH\_RD experiments (Fig. 13).  
450 In general, lower score metrics are obtained when a higher threshold for precipitation forecasts is  
451 evaluated, likely resulting from a lower frequency of occurrence for heavy precipitation. As seen in the  
452 CREF forecast, the FH\_RD, RD, and FH experiments show more skillful precipitation forecasts than  
453 CTL does. In terms of the 2.5-mm precipitation forecast, FH\_RD generally achieves the highest POD,  
454 SR, CSI, and ETS, along with the smallest BIAS, with RD exhibiting slightly inferior performance (Fig.  
455 13a and b). For the 5-mm threshold, FH generates the highest POD and ETS in the first 3 hours,  
456 whereas RD delivers the lowest FAR and largest ETS in the subsequent 3-h forecasts (Fig. 13c and d).  
457 The RD experiment outperforms all the other experiments in the 1-, 3-, and 4-h forecasts at the  
458 threshold of 10 mm (Fig. 13e and f). One possible reason for the inferior performance of FH\_RD and  
459 FH compared to RD at higher thresholds is that FH\_RD exhibits a slight southward displacement error  
460 for the 1-3 h heavier precipitation (>10 mm) forecasts in southwestern Beijing compared to the truth  
461 simulation, while the precipitation in the FH experiment is located further north (Fig. 11a-b, 11g-h vs.  
462 Fig. 10a-b). This may lead to larger penalties in the calculation of POD and ETS, resulting in lower  
463 scores.



464

465

466

**Figure 13.** Same as in Fig. 12, but for 1-6 h hourly precipitation amount (HPRCP) forecasts for case 1 at thresholds of 2.5 mm (1st row), 5 mm (2nd row), and 10 mm (3rd row), respectively.

467

#### 4.1.3 Sensitivity to vertical resolution and detection height

468

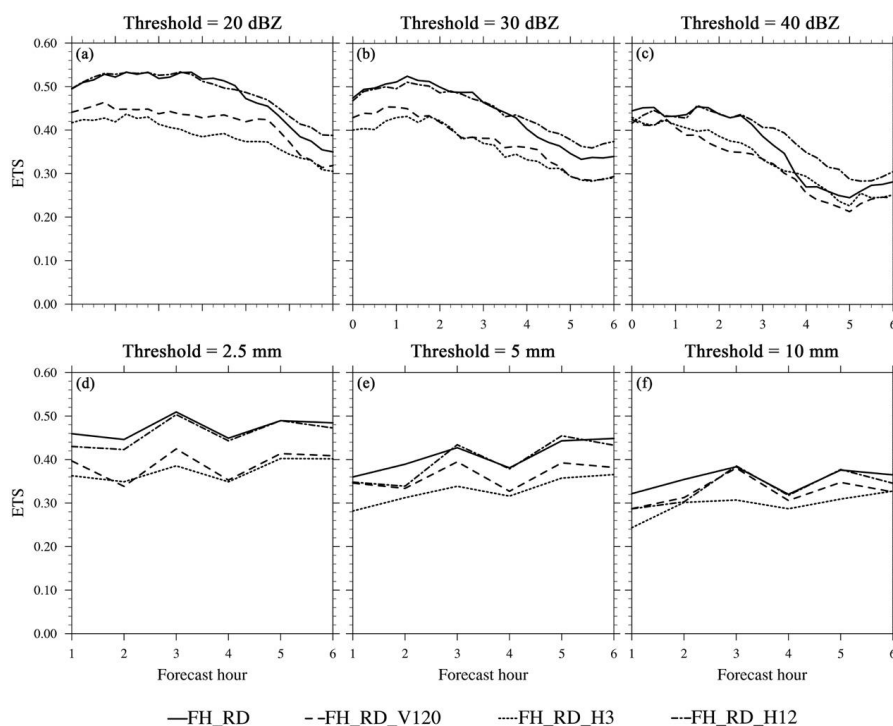
469

470

Given the encouraging preliminary results from the FH\_RD experiment, ETS figures of CREF and HPRCP forecasts from three additional sensitivity experiment—FH\_RD\_V120, FH\_RD\_H3, and FH\_RD\_H12—are compared to examine the relative impact of different vertical resolutions and



471 maximum detection heights on the analyses and forecasts (Fig. 14). For reflectivity forecasts at  
 472 thresholds of 20–40 dBZ, the 0–3 h ETSs of FH\_RD and FH\_RD\_H12 are comparable. However, the  
 473 FH\_RD\_H12 experiment achieves higher forecast scores after 3 hours, highlighting the benefit of a  
 474 higher detection height (Fig. 14a–c). Conversely, the FH\_RD\_H3 experiment (with the lowest detection  
 475 height of 3 km) shows the smallest ETS values at 20 and 30 dBZ, while FH\_RD\_V120 (with a lower  
 476 vertical resolution of 120 m) demonstrates the poorest forecast skill at 40 dBZ. Consistent with the  
 477 CREF forecast, both FH\_RD and FH\_RD\_H12 show more skillful HPRCP forecasts than  
 478 FH\_RD\_V120 and FH\_RD\_H3. However, the ETSs of FH\_RD are higher than those of FH\_RD\_H12  
 479 at most forecast lead times, which differs from the reflectivity results. Additionally, FH\_RD\_H3  
 480 produces the lowest ETS values throughout the 0–6 h forecasts at thresholds of 2.5–10 mm. Generally,  
 481 the higher the maximum detection height of RWPs and the denser the vertical distribution of  
 482 observations, the more significant the positive impact of RWP DA in terms of ETS. Moreover, a  
 483 maximum detection height of 8 km seems to be a reasonable and effective choice, while the reduction  
 484 of vertical resolution from 60 m to 120 m has less impact compared to the effect of decreasing the  
 485 detection altitude to 3 km.



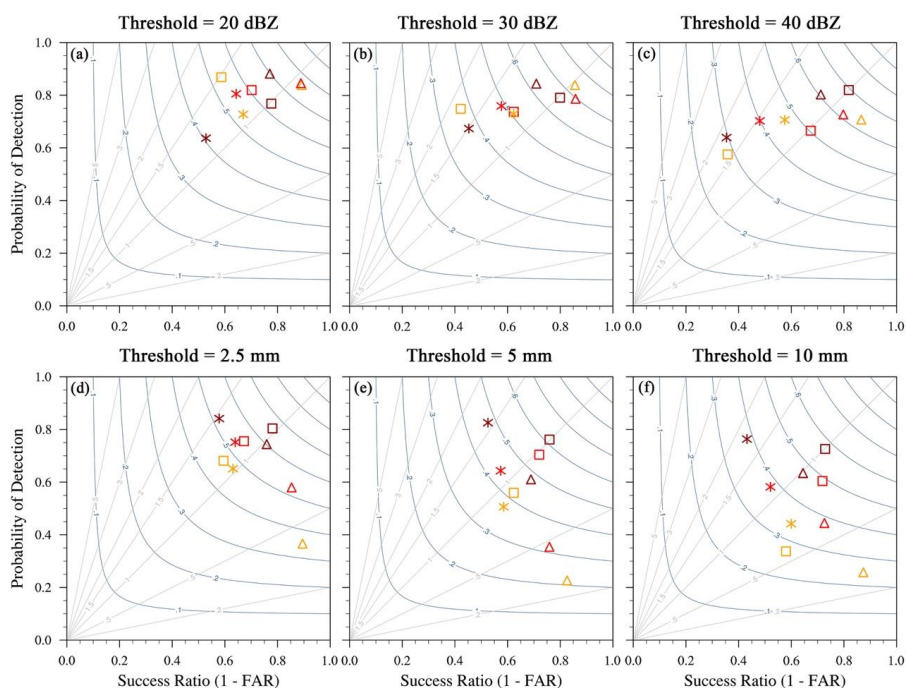
486



487 **Figure 14.** Equitable threat score (ETS) for 0-6 h CREF forecasts from the FH\_RD (solid),  
488 FH\_RD\_V120 (dashed), FH\_RD\_H3 (dotted), and FH\_RD\_H12 (dashdot) experiments for case 1 at  
489 thresholds of (a) 20, (b) 30, and (c) 40 dBZ, respectively. (d–f) Same as in (a–c), but for 1-6 h HPRCP  
490 forecasts from each experiment at thresholds of (d) 2.5, (e) 5, and (f) 10 mm, respectively.

#### 491 **4.2 Aggregate forecast performance**

492         Considering the variations in weather scenarios and storm environments across cases, we also  
493 examined two additional SW-type heavy rainfall events that occurred over the Beijing-Tianjin-Hebei  
494 region on 28 June and 12 July 2023 to evaluate the impact of RWPs observed from different spatial  
495 layouts on short-term forecasts. Despite the presence of a southwesterly jet stream in all three cases,  
496 they produced distinct storm modes under different weather conditions. To delve deeper into the  
497 verification metrics from the three cases, we present performance diagrams of CREF and HPRCP  
498 forecasts from the FH\_RD experiment as the best assimilation experiment (Fig. 15). Except for 28 June  
499 2023, the BIAS values fall within a reasonable range of 0.8–1.5 for reflectivity and 0.8–1.7 for  
500 precipitation, indicating overall good forecast performance. The forecast skills generally exhibit lower  
501 score metrics and more variability at higher thresholds. However, some of the forecast scores do not  
502 decrease monotonically with increasing forecast lead time. For 12 July 2023, smaller BIAS and FAR  
503 values are obtained for the 3- and 6-h reflectivity and precipitation forecasts, along with higher CSI.  
504 This occurs due to several factors: (a) initial scattered convection develops into a larger-scale west-east  
505 oriented system covering all of Beijing and central-northern Hebei at later times in this case, which  
506 models usually capture better; (b) errors in the timing and location of CI become less significant as  
507 convection evolves and forms clearer structures; and (c) for the free forecasts initialized from the first  
508 few hours, convection may not have started until the final forecast hour. CREF forecasts from 28 June  
509 2023 show the best performance in terms of high POD, SR, and CSI. Nevertheless, persistent  
510 underprediction throughout the 1–6 h precipitation forecasts at all thresholds from this case can mostly  
511 be traced back to the difficulty in forecasting small-scale, short-lived, and relatively weak precipitation  
512 events.

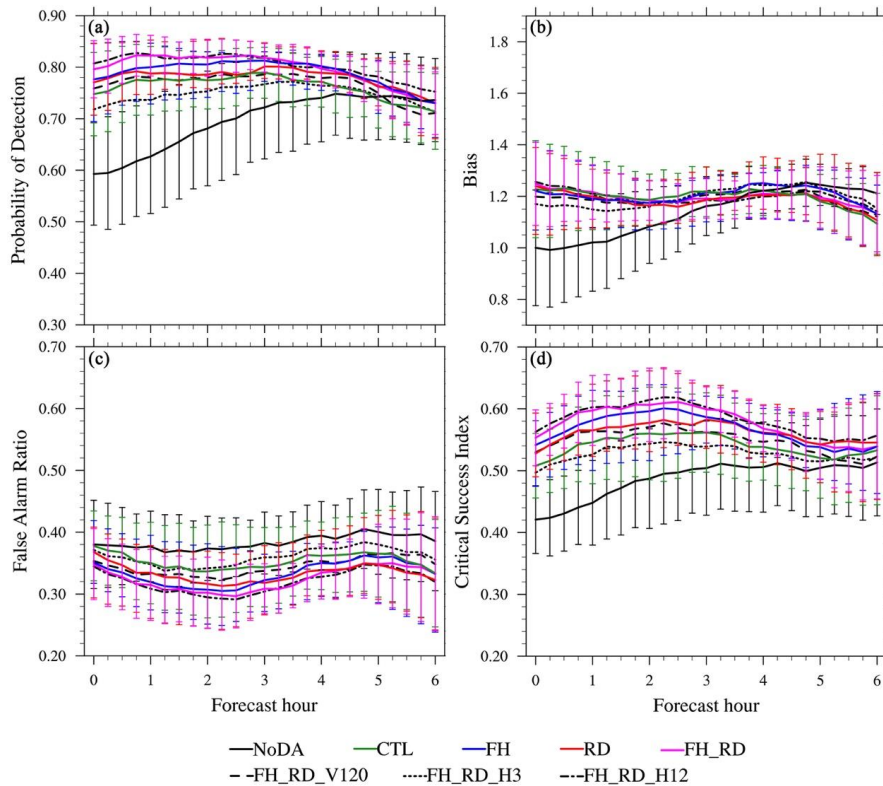


513  $\Delta$  20230628  $\square$  20230712  $*$  20230721  
514 **Figure 15.** Performance diagram for 0-6 h CREF forecasts from the FH\_RD experiment in each case at  
515 thresholds of (a) 20, (b) 30, and (c) 40 dBZ, respectively. (d-f) Same as in (a-c), but for 1-6 h HPRCP  
516 forecasts from each case at thresholds of (d) 2.5, (e) 5, and (f) 10 mm, respectively. Orange, red, and  
517 brown colors denote the forecast hour of 0- (1- for precipitation forecast), 3-, and 6-hr. Results are  
518 shown for a neighborhood radius of 12-km.

519 To gain a comprehensive view of assimilating RWPs from multiple networks, quantitative  
520 verification parameters (POD, BIAS, FAR, and CSI) from each case are aggregated across all available  
521 forecast times. Figures 16 and 17 display time series of aggregated metrics for CREF forecasts from  
522 NoDA, CTL, FH, RD, FH\_RD, FH\_RD\_V120, FH\_RD\_H3, and FH\_RD\_H12 experiments at 20- and  
523 40-dBZ thresholds, respectively. The error bars for NoDA, CTL, FH, RD, and FH\_RD in the graphs  
524 represent a 95% confidence interval. Compared to NoDA, all DA experiments exhibit more skillful 0-  
525 6h reflectivity forecasts, with higher POD and CSI, smaller FAR, and BIAS closer to unity (statistically  
526 significant at 95% confidence level in the first 3 hours). Among CTL, FH, RD, and FH\_RD, FH\_RD  
527 consistently outperforms others, showing the highest POD values across all forecast hours (Fig. 16a). A  
528 slight overprediction bias (1.1-1.2) is observed for all DA experiments at all forecast times (Fig. 16b).



529 CTL exhibits the largest BIAS in the first 3 hours, while FH's BIAS increases to 1.2 over time. FH\_RD  
 530 shows the steepest decrease in FAR, indicating the most effective reduction in false alarms (Fig. 16c).  
 531 CTL remains relatively flat and maintains the highest FAR among the four DA experiments throughout  
 532 the 0–6h forecasts. The FARs for FH and RD forecasts fall between those of FH\_RD and CTL.  
 533 Specifically, FH has a lower FAR in the first 3 hours, whereas in the next 3 hours, RD performs better.  
 534 Similar trend is also evident in CSI values over time (Fig. 16d). In conclusion, FH\_RD consistently  
 535 performs best overall across all metrics, followed by RD and FH. CTL underperforms, with less  
 536 improvement in score metrics. Sensitivity tests show FH\_RD\_H12 performs slightly better than  
 537 FH\_RD, while FH\_RD\_H3 shows the least improvement. FH\_RD\_V120 falls between FH\_RD\_H12  
 538 and FH\_RD\_H3, consistent with the single-case study in Sect. 4.1.3.



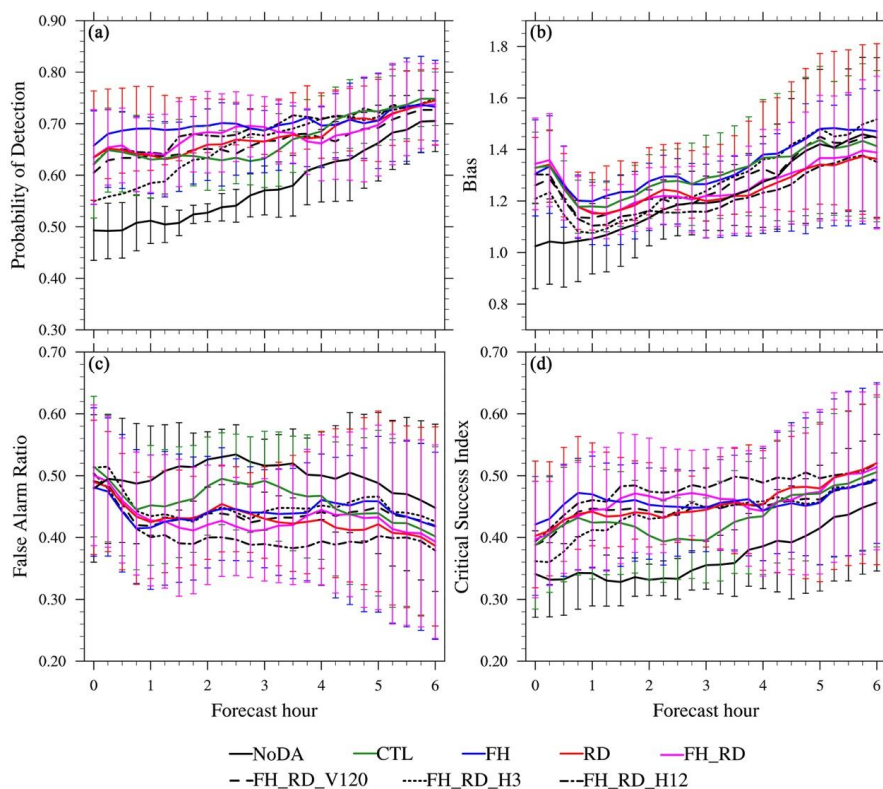
539  
 540 **Figure 16.** Time series of (a) Probability of detection (POD), (b) Bias, (c) false alarm ratio (FAR), and  
 541 (d) critical success index (CSI) for CREF forecasts aggregated from each initialization hour from the  
 542 sixth hour to the end of DA cycles across three cases (June 28, July 12, July 21 of 2023) at the  
 543 threshold of 20 dBZ for the NoDA (black solid), CTL (green solid), FH (blue solid), RD (red solid),  
 FH\_RD (purple solid), FH\_RD\_V120 (black dashed), FH\_RD\_H3 (green dashed), and FH\_RD\_H12 (red dashed).



544 FH\_RD (magenta solid), FH\_RD\_V120 (black dashed), FH\_RD\_H3 (black dotted), and FH\_RD\_H12  
545 (black dashdot) experiments. Results are shown for a neighborhood radius of 12-km. Error bars for  
546 NoDA, CTL, FH, RD, and FH\_RD experiments represent a 95% confidence interval.

547         Similar to the 20-dBZ reflectivity forecast, RWP DA experiments outperform NoDA at 40-dBZ,  
548 although only the POD result in the first 3 hours is statistically significant at the 95% confidence level.  
549 All DA experiments exhibit an overprediction bias (1.1–1.5) throughout the 0–6 h forecasts (Fig. 17b).  
550 Notably, FH shows the highest bias. However, FH also exhibits the highest POD in the first 2 hours and  
551 highest CSI and lowest FAR in the first hour. Subsequently, FH\_RD and RD perform better, with  
552 FH\_RD slightly outperforming RD in 1–3 h forecasts and RD performing better in 4–6 hours. The  
553 different impacts of ridge and foothill networks may be attributed to: a) Dynamic forcing of terrain,  
554 which has a delayed effect on triggering and intensifying storms, leading to improved forecasts for  
555 later-occurring storms. b) Assimilating wind observations at foothills, capturing local southwesterly  
556 flow characteristics, enhances forecasts of initial moisture lifting and convection triggering. During the  
557 first 45 minutes, strong overprediction leads to high POD and FAR, which quickly decline as the  
558 forecast progresses (Fig. 17a and c). This contributes to an increase in CSI (Fig. 17d). A possible reason  
559 is that the model requires time (several minutes to an hour) to digest and adjust to assimilated wind  
560 information. The impact of vertical resolution and detection height on 40-dBZ reflectivity forecasts is  
561 consistent with the results observed at the 20-dBZ threshold.





562

563 **Figure 17.** Same as in Figure 16, but for CREF forecasts at the threshold of 40 dBZ.

564

565

566

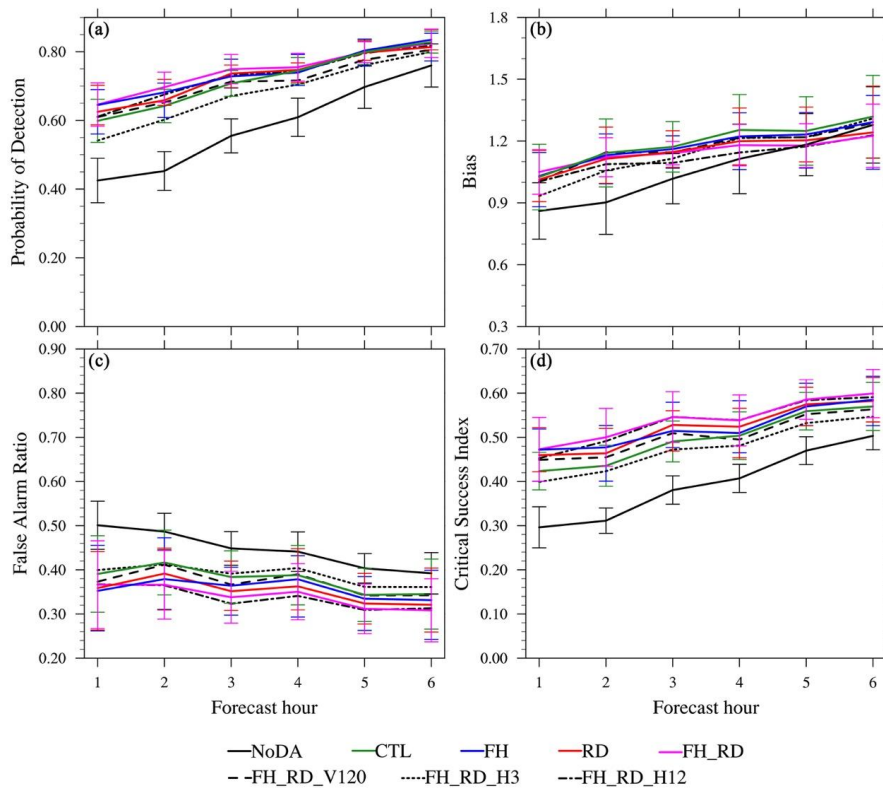
567

568

569

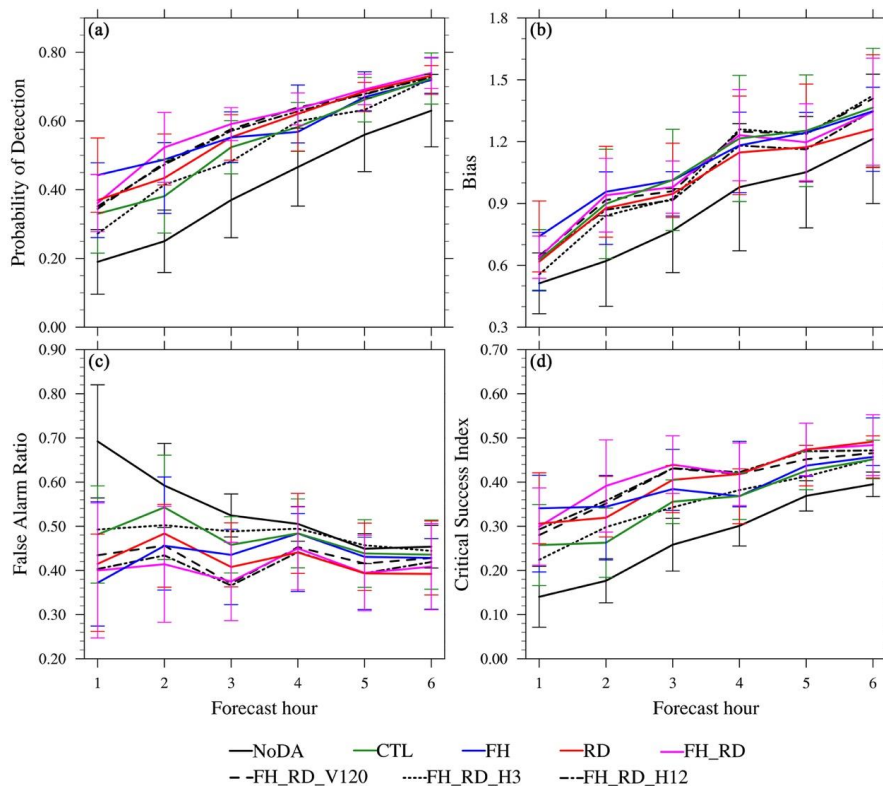
570

Consistent with the 20-dBZ reflectivity forecast, FH\_RD and FH\_RD\_H12 consistently achieve the best performance across all score metrics in HPRCP forecasts, followed by RD and FH (Fig. 18 and 19). Although the improvements are not statistically significant at the 95% confidence level, FH\_RD and FH\_RD\_H12 exhibit added forecast skill over the NoDA experiment. In contrast, CTL and FH\_RD\_H3 show minimal improvement across all metrics. At 10-mm threshold, FH produces higher forecast scores than the others in the first hour, while FH\_RD and RD show superiority in 2–4 h and 4–6 h, respectively (Fig. 19).



571

572 **Figure 18.** Same as in Figure 16, but for 1-6 h HPRCP forecasts aggregated from three cases at the  
573 thresholds of 2.5 mm.



574

575 **Figure 19.** Same as in Figure 18, but for precipitation forecasts at the threshold of 10 mm.

576 **5. Summary and conclusions**

577 In this research, observing system simulation experiments are performed to study the benefits of  
578 assimilating RWP observations for forecasting CI along small-scale boundary layer convergence zones.  
579 Synthetic RWP observations are assimilated into the WRF model using the NSSL3DVAR DA system  
580 for three SW-type heavy rainfall events that occurred over the Beijing-Tianjin-Hebei region. To  
581 investigate the impact of RWP data observed from multiple networks on convective scale short-term  
582 forecasts, the background run (NoDA), which does not assimilate any observations, and four types of  
583 DA experiments are carried out. A baseline experiment (CTL), which assimilates RWPs from the  
584 operational network alone, is first performed and serves as a benchmark for comparison with  
585 subsequent DA experiments. The FH and RD experiments assimilate simulated RWP observations from  
586 the foothill and ridge networks of the Taihang Mountains in addition to the operational network. The



587 FH\_RD experiment is conducted by assimilating combined RWP data from the operational, foothill,  
588 and ridge sites. Comparison of analyses and forecasts from these four types of experiments reveals  
589 improvements in model initial conditions and short-term severe weather forecasts by assimilating  
590 simulated RWP observations, as well as the added value of RWPs from the foothill and ridge networks  
591 over operational network data. Furthermore, three sensitivity DA experiments (FH\_RD\_V120,  
592 FH\_RD\_H3, and FH\_RD\_H12) are carried out to test the impact of vertical resolution and maximum  
593 detection heights. The purpose of these experiments is to investigate a potential optimal configuration  
594 for the vertical data availability of real-time RWPs to be assimilated in future convective scale NWP.  
595 For each DA experiment, the analysis is cycled for 9 hours at 15-min intervals, with a 6-h free forecast  
596 initiated every hour starting from the sixth hour of the analysis cycles. First of all, both subjective and  
597 objective verifications of the analysis and forecast were performed in detail for the 21 July 2023 case.  
598 Then statistical metrics, including neighborhood-based POD, FAR, BIAS, and CSI of reflectivity and  
599 precipitation forecasts, were aggregated from each initialization hour across the three cases. The main  
600 results are summarized as follows:

601 1) Comparison of wind analyses and forecasts among the CTL, FH, RD, and FH\_RD  
602 experiments reveals that the FH\_RD experiment yields the smallest wind errors, both in terms of  
603 the overall domain average and the vertical profile of RMSEs for wind components. Then, it is  
604 followed by RD, then FH, with CTL exhibiting the largest wind errors. A qualitative evaluation of  
605 the model's initial mesoscale dynamics indicates that the assimilation of RWP data successfully  
606 corrects the wind direction and speed biases in Beijing and its surrounding areas, enhancing the  
607 southwesterly jet. Moreover, both RD and FH\_RD (with the assimilation of RWP data from the  
608 ridge network) remarkably reduce large wind errors in the upstream of Beijing along the  
609 mountains, which is crucial for CI in the vicinity of the boundary between Hebei and southwestern  
610 Beijing.

611 2) For the 21 July 2023 event, qualitative verification focused on the convective system  
612 initiated southwest of Beijing, which intensified after merging with storms from western Hebei,  
613 forming a prominent southwest-northeast oriented system across Beijing. The NoDA experiment  
614 initially underestimates convection in Beijing and Hebei but overpredicts storm coverage and  
615 intensity in later forecasts, generating excessive spurious convection. All RWP DA experiments  
616 enhance CI timing and location by capturing mesoscale flow features, subsequently reducing storm



617 displacement and intensity errors. Nevertheless, the CTL experiment underestimates storm  
618 intensity, while FH still retains some spurious echoes in forecasts. Overall, the FH\_RD experiment  
619 demonstrates significant superiority in areal coverage, storm mode, and orientation compared to  
620 the other DA experiments. The accumulated precipitation forecasts show similar trends to the  
621 reflectivity results regarding rainfall location, onset time, and amount. The forecast statistics  
622 indicate that FH\_RD achieves the best performance in reflectivity and precipitation forecasts at  
623 lower thresholds (i.e., 20- and 30-dBZ for CREF, and 2.5-mm for HPRCP), whereas the RD  
624 experiment slightly surpasses FH\_RD at the 50-dBZ and 10-mm thresholds. The lower  
625 performance of FH\_RD and FH at higher thresholds may be linked to slight displacement errors in  
626 heavy precipitation forecasts, impacting their POD and ETS scores.

627 3) Quantitative verification results aggregated across the three SW-type heavy rainfall  
628 cases in the Beijing-Tianjin-Hebei region confirm that FH\_RD exhibits the best performance in  
629 reflectivity and precipitation forecasts, followed by RD and FH, while CTL shows minimal  
630 improvement. An exception is that at higher thresholds, FH achieves the best scores in the first 1 or  
631 2 hours despite stronger overprediction, while FH\_RD and RD are superior in subsequent hours.  
632 This is potentially attributed to the delayed effect of dynamic forcing from the terrain, as well as  
633 improvements in capturing the initial southwesterly flow and local convection by assimilating  
634 wind observations at the foothills. In addition, the results from sensitivity experiments on vertical  
635 resolution and maximum detection height indicate that FH\_RD\_H12 exhibits comparable or  
636 slightly better performance compared to FH\_RD, benefiting from its higher detection height.  
637 Conversely, the FH\_RD\_H3 experiment, with the lowest detection height, has the poorest forecast  
638 skills among all DA experiments, while FH\_RD\_V120 generally falls between FH\_RD\_H12 and  
639 FH\_RD\_H3.

640 The results consistently demonstrate that the FH\_RD experiment, combining data from ridge,  
641 foothill, and operational wind profiler networks, delivers the most accurate short-term forecasts.  
642 Specifically, the assimilation of RWP data from ridge network significantly reduces wind errors in  
643 complex terrain, such as the Taihang Mountains upstream of Beijing. These regions are critical for  
644 convective initiation in Beijing and its surroundings. The findings highlight the essential role of  
645 integrating both ridge and foothill data in improving overall reflectivity and precipitation forecasts over  
646 the Beijing-Tianjin-Hebei region. Sensitivity experiments on vertical resolution and detection height



647 further emphasize the importance of high vertical resolution and maximizing detection height in  
648 optimizing the RWP network for enhanced forecast accuracy.

649 The insights gained from this OSSE study on the impacts of RWP observations on heavy rainfall  
650 forecasting will inform the design of optimal RWP networks over the Beijing-Tianjin-Hebei region.  
651 This preliminary study lays the groundwork for further research to fully understand the complexities of  
652 precipitation forecasting related to data assimilation. The current investigation focused on three  
653 SW-type heavy rainfall cases occurring in summer over the Beijing-Tianjin-Hebei region, utilizing  
654 model-simulated states and observational networks. Future research directions include: (1) Expanding  
655 the study to other precipitation types and high-impact convective events under diverse weather  
656 scenarios. (2) Investigating the benefits of assimilating real observational data on convective scale  
657 NWP once proposed RWP networks become available. Moreover, future studies can address the  
658 limitations of static background errors in 3DVAR by incorporating flow-dependent background error  
659 covariances estimated from ensemble forecasts.

660

#### 661 **Code and data availability**

662 The source codes of WRF model version 3.7.1 could be downloaded after filling in the E-mail address  
663 ([https://www2.mmm.ucar.edu/wrf/users/download/get\\_source.html](https://www2.mmm.ucar.edu/wrf/users/download/get_source.html)). The ERA5 reanalysis and GFS  
664 forecast data are accessible from ECMWF  
665 (<https://www.ecmwf.int/en/forecasts/datasets/reanalysis-datasets/era5/>) and National Centers for  
666 Environmental Prediction, National Weather Service, NOAA, U.S. Department of Commerce (2015),  
667 respectively.

668

#### 669 **Author contributions**

670 JZ and JG conceptualized the study. JZ executed the experiments, analyzed the results, and wrote the  
671 paper. JG supervised the project, provided critical feedback during the experiment implementation stage,  
672 and revised the paper. XZ assisted in the analysis and visualizations.

673

#### 674 **Competing interests**

675 The contact author has declared that none of the authors has any competing interests.

676



677 **Disclaimer**

678 Publisher's note: Copernicus Publications remains neutral with regard to jurisdictional claims in  
679 published maps and institutional affiliations.

680

681 **Acknowledgements**

682 This work was jointly supported by the National Natural Science Foundation of China (U2142209,  
683 42325501 and 42375018), and the China Meteorological Administration Training Centre Key Research  
684 Program (2023CMATCZDIAN08). Dr. Jidong Gao kindly provided internal review which led to  
685 improvement of the manuscript. ChatGPT (GPT-4; OpenAI's large-scale language-generation model)  
686 was used to improve the writing style of this article.



687 **References**

- 688 Benjamin, S. G., Grell, G. A., Brown, J. M., Smirnova, T. G., and Bleck, R.: Mesoscale Weather  
689 Prediction with the RUC Hybrid Isentropic–Terrain-Following Coordinate Model, *Monthly*  
690 *Weather Review*, 132, 473–494,  
691 [https://doi.org/10.1175/1520-0493\(2004\)132<0473:MWPWTR>2.0.CO;2](https://doi.org/10.1175/1520-0493(2004)132<0473:MWPWTR>2.0.CO;2), 2004a.
- 692 Benjamin, S. G., Schwartz, B. E., Szoke, E. J., and Koch, S. E.: The Value of Wind Profiler Data  
693 in U.S. Weather Forecasting, *Bulletin of the American Meteorological Society*, 85, 1871–1886,  
694 <https://doi.org/10.1175/BAMS-85-12-1871>, 2004b.
- 695 Bouttier, F.: The use of profiler data at ECMWF, *metz*, 10, 497–510,  
696 <https://doi.org/10.1127/0941-2948/2001/0010-0497>, 2001.
- 697 Bucci, L. R., Majumdar, S. J., Atlas, R., Emmitt, G. D., and Greco, S.: Understanding the response  
698 of tropical cyclone structure to the assimilation of synthetic wind profiles, *Monthly Weather*  
699 *Review*, <https://doi.org/10.1175/MWR-D-20-0153.1>, 2021.
- 700 Clark, A. J., Gallus, W. A., and Weisman, M. L.: Neighborhood-Based Verification of Precipitation  
701 Forecasts from Convection-Allowing NCAR WRF Model Simulations and the Operational NAM,  
702 *Weather and Forecasting*, 25, 1495–1509, <https://doi.org/10.1175/2010WAF2222404.1>, 2010.
- 703 Dudhia, J.: Numerical Study of Convection Observed during the Winter Monsoon Experiment  
704 Using a Mesoscale Two-Dimensional Model, *Journal of Atmospheric Sciences*, 46, 3077–3107,  
705 [https://doi.org/10.1175/1520-0469\(1989\)046<3077:NSOCOD>2.0.CO;2](https://doi.org/10.1175/1520-0469(1989)046<3077:NSOCOD>2.0.CO;2), 1989.
- 706 Dunn, L.: An Example of Subjective Interpretation of Network Profiler Data in Real-Time  
707 Forecasting, *Weather and Forecasting*, 1, 219–225,  
708 [https://doi.org/10.1175/1520-0434\(1986\)001<0219:AEOSIO>2.0.CO;2](https://doi.org/10.1175/1520-0434(1986)001<0219:AEOSIO>2.0.CO;2), 1986.
- 709 Fierro, A. O., Gao, J., Ziegler, C. L., Calhoun, K. M., Mansell, E. R., and MacGorman, D. R.:  
710 Assimilation of Flash Extent Data in the Variational Framework at Convection-Allowing Scales:  
711 Proof-of-Concept and Evaluation for the Short-Term Forecast of the 24 May 2011 Tornado  
712 Outbreak, *Monthly Weather Review*, 144, 4373–4393, <https://doi.org/10.1175/MWR-D-16-0053.1>,  
713 2016.
- 714 Fierro, A. O., Wang, Y., Gao, J., and Mansell, E. R.: Variational Assimilation of Radar Data and  
715 GLM Lightning-Derived Water Vapor for the Short-Term Forecasts of High-Impact Convective  
716 Events, *Monthly Weather Review*, 147, 4045–4069, <https://doi.org/10.1175/MWR-D-18-0421.1>,  
717 2019.
- 718 Gao, J. and Stensrud, D. J.: Some Observing System Simulation Experiments with a Hybrid  
719 3DEnVAR System for Storm-Scale Radar Data Assimilation, *Monthly Weather Review*, 142,  
720 3326–3346, <https://doi.org/10.1175/MWR-D-14-00025.1>, 2014.
- 721 Gao, J., Xue, M., Brewster, K., and Drogemeier, K. K.: A Three-Dimensional Variational Data  
722 Analysis Method with Recursive Filter for Doppler Radars, *Journal of Atmospheric and Oceanic*





- 723 Technology, 21, 457–469,  
724 [https://doi.org/10.1175/1520-0426\(2004\)021<0457:ATVDAM>2.0.CO;2](https://doi.org/10.1175/1520-0426(2004)021<0457:ATVDAM>2.0.CO;2), 2004.
- 725 Gao, J., Smith, T. M., Stensrud, D. J., Fu, C., Calhoun, K., Manross, K. L., Brogden, J.,  
726 Lakshmanan, V., Wang, Y., Thomas, K. W., Brewster, K., and Xue, M.: A Real-Time  
727 Weather-Adaptive 3DVAR Analysis System for Severe Weather Detections and Warnings,  
728 *Weather and Forecasting*, 28, 727–745, <https://doi.org/10.1175/WAF-D-12-00093.1>, 2013.
- 729 Gao, J., Fu, C., Stensrud, D. J., and Kain, J. S.: OSSEs for an Ensemble 3DVAR Data Assimilation  
730 System with Radar Observations of Convective Storms, *Journal of the Atmospheric Sciences*, 73,  
731 2403–2426, <https://doi.org/10.1175/JAS-D-15-0311.1>, 2016.
- 732 Gao, J., Heinselman, L. P., Xue, M., Wicker, L. J., Yussouf, N., Stensrud, D. J., and Droegemeier,  
733 K. K.: The Numerical Prediction of Severe Convective Storms: Advances in Research and  
734 Applications, Remaining Challenges, and Outlook for the Future., in: *Encyclopedia of*  
735 *Atmospheric Sciences*, Elsevier, 2024.
- 736 Guo, X., Guo, J., Zhang, D., and Yun, Y.: Vertical divergence profiles as detected by two wind-  
737 profiler mesonets over East China: Implications for nowcasting convective storms, *Quart J Royal*  
738 *Meteoro Soc*, 149, 1629–1649, <https://doi.org/10.1002/qj.4474>, 2023.
- 739 Heinselman, P. L., Burke, P. C., Wicker, L. J., Clark, A. J., Kain, J. S., Gao, J., Yussouf, N., Jones,  
740 T. A., Skinner, P. S., Potvin, C. K., Wilson, K. A., Gallo, B. T., Flora, M. L., Martin, J., Creager, G.,  
741 Knopfmeier, K. H., Wang, Y., Matilla, B. C., Dowell, D. C., Mansell, E. R., Roberts, B.,  
742 Hoogewind, K. A., Stratman, D. R., Guerra, J., Reinhart, A. E., Kerr, C. A., and Miller, W.:  
743 Warn-on-Forecast System: From Vision to Reality, *Weather and Forecasting*, 39, 75–95,  
744 <https://doi.org/10.1175/WAF-D-23-0147.1>, 2024.
- 745 Hersbach, H., Bell, B., Berrisford, P., Hirahara, S., Horányi, A., Muñoz-Sabater, J., Nicolas, J.,  
746 Peubey, C., Radu, R., Schepers, D., Simmons, A., Soci, C., Abdalla, S., Abellan, X., Balsamo, G.,  
747 Bechtold, P., Biavati, G., Bidlot, J., Bonavita, M., De Chiara, G., Dahlgren, P., Dee, D.,  
748 Diamantakis, M., Dragani, R., Flemming, J., Forbes, R., Fuentes, M., Geer, A., Haimberger, L.,  
749 Healy, S., Hogan, R. J., Hólm, E., Janisková, M., Keeley, S., Laloyaux, P., Lopez, P., Lupu, C.,  
750 Radnoti, G., De Rosnay, P., Rozum, I., Vamborg, F., Villaume, S., and Thépaut, J.: The ERA5  
751 global reanalysis, *Quart J Royal Meteoro Soc*, 146, 1999–2049, <https://doi.org/10.1002/qj.3803>,  
752 2020.
- 753 Hoffmann, L., Günther, G., Li, D., Stein, O., Wu, X., Griessbach, S., Heng, Y., Konopka, P.,  
754 Müller, R., Vogel, B., and Wright, J. S.: From ERA-Interim to ERA5: the considerable impact of  
755 ECMWF’s next-generation reanalysis on Lagrangian transport simulations, *Atmos. Chem. Phys.*,  
756 19, 3097–3124, <https://doi.org/10.5194/acp-19-3097-2019>, 2019.
- 757 Hong, S.-Y., Noh, Y., and Dudhia, J.: A New Vertical Diffusion Package with an Explicit  
758 Treatment of Entrainment Processes, *Monthly Weather Review*, 134, 2318–2341,  
759 <https://doi.org/10.1175/MWR3199.1>, 2006.



- 760 Hu, H., Sun, J., and Zhang, Q.: Assessing the Impact of Surface and Wind Profiler Data on Fog  
761 Forecasting Using WRF 3DVAR: An OSSE Study on a Dense Fog Event over North China,  
762 Journal of Applied Meteorology and Climatology, 56, 1059–1081,  
763 <https://doi.org/10.1175/JAMC-D-16-0246.1>, 2017.
- 764 Hu, J., Fierro, A. O., Wang, Y., Gao, J., and Mansell, E. R.: Exploring the Assimilation of  
765 GLM-Derived Water Vapor Mass in a Cycled 3DVAR Framework for the Short-Term Forecasts of  
766 High-Impact Convective Events, Monthly Weather Review, 148, 1005–1028,  
767 <https://doi.org/10.1175/MWR-D-19-0198.1>, 2020.
- 768 Huang, Y., Wang, X., Kerr, C., Mahre, A., Yu, T.-Y., and Bodine, D.: Impact of Assimilating  
769 Future Clear-Air Radial Velocity Observations from Phased-Array Radar on a Supercell  
770 Thunderstorm Forecast: An Observing System Simulation Experiment Study, Monthly Weather  
771 Review, 148, 3825–3845, <https://doi.org/10.1175/MWR-D-19-0391.1>, 2020.
- 772 Huang, Y., Wang, X., Mahre, A., Yu, T.-Y., and Bodine, D.: Impacts of assimilating future clear-air  
773 radial velocity observations from phased array radar on convection initiation forecasts: An  
774 observing system simulation experiment study, Monthly Weather Review,  
775 <https://doi.org/10.1175/MWR-D-21-0199.1>, 2022.
- 776 Huo, Z., Liu, Y., Shi, Y., Chen, B., Fan, H., and Li, Y.: An Investigation on Joint Data Assimilation  
777 of a Radar Network and Ground-Based Profiling Platforms for Forecasting Convective Storms,  
778 Monthly Weather Review, 151, 2049–2064, <https://doi.org/10.1175/MWR-D-22-0332.1>, 2023.
- 779 Ishihara, M., Kato, Y., Abo, T., Kobayashi, K., and Izumikawa, Y.: Characteristics and  
780 Performance of the Operational Wind Profiler Network of the Japan Meteorological Agency,  
781 Journal of the Meteorological Society of Japan, 84, 1085–1096,  
782 <https://doi.org/10.2151/jmsj.84.1085>, 2006.
- 783 Jones, T. A., Wang, X., Skinner, P., Johnson, A., and Wang, Y.: Assimilation of GOES-13 Imager  
784 Clear-Sky Water Vapor (6.5  $\mu\text{m}$ ) Radiances into a Warn-on-Forecast System, Monthly Weather  
785 Review, 146, 1077–1107, <https://doi.org/10.1175/MWR-D-17-0280.1>, 2018.
- 786 Lai, A., Gao, J., Koch, S. E., Wang, Y., Pan, S., Fierro, A. O., Cui, C., and Min, J.: Assimilation of  
787 Radar Radial Velocity, Reflectivity, and Pseudo-Water Vapor for Convective-Scale NWP in a  
788 Variational Framework, Monthly Weather Review, 147, 2877–2900,  
789 <https://doi.org/10.1175/MWR-D-18-0403.1>, 2019.
- 790 Li, N., Guo, J., Wu, M., Zhang, F., Guo, X., Sun, Y., Zhang, Z., Liang, H., and Chen, T.:  
791 Low-Level Jet and Its Effect on the Onset of Summertime Nocturnal Rainfall in Beijing,  
792 Geophysical Research Letters, 51, e2024GL110840, <https://doi.org/10.1029/2024GL110840>,  
793 2024.
- 794 Liu, B., Guo, J., Gong, W., Shi, L., Zhang, Y., and Ma, Y.: Characteristics and performance of  
795 wind profiles as observed by the radar wind profiler network of China, Atmos. Meas. Tech., 13,  
796 4589–4600, <https://doi.org/10.5194/amt-13-4589-2020>, 2020.



- 797 Liu, D., Huang, C., and Feng, J.: Influence of Assimilating Wind Profiling Radar Observations in  
798 Distinct Dynamic Instability Regions on the Analysis and Forecast of an Extreme Rainstorm Event  
799 in Southern China, *Remote Sensing*, 14, 3478, <https://doi.org/10.3390/rs14143478>, 2022.
- 800 Mansell, E. R. and Ziegler, C. L.: Aerosol Effects on Simulated Storm Electrification and  
801 Precipitation in a Two-Moment Bulk Microphysics Model, *Journal of the Atmospheric Sciences*,  
802 70, 2032–2050, <https://doi.org/10.1175/JAS-D-12-0264.1>, 2013.
- 803 Mansell, E. R., Ziegler, C. L., and Bruning, E. C.: Simulated Electrification of a Small  
804 Thunderstorm with Two-Moment Bulk Microphysics, *Journal of the Atmospheric Sciences*, 67,  
805 171–194, <https://doi.org/10.1175/2009JAS2965.1>, 2010.
- 806 Mlawer, E. J., Taubman, S. J., Brown, P. D., Iacono, M. J., and Clough, S. A.: Radiative transfer  
807 for inhomogeneous atmospheres: RRTM, a validated correlated-k model for the longwave, *J.*  
808 *Geophys. Res.*, 102, 16663–16682, <https://doi.org/10.1029/97JD00237>, 1997.
- 809 Pan, S., Gao, J., Stensrud, D. J., Wang, X., and Jones, T. A.: Assimilation of Radar Radial Velocity  
810 and Reflectivity, Satellite Cloud Water Path, and Total Precipitable Water for Convective-Scale  
811 NWP in OSSEs, *Journal of Atmospheric and Oceanic Technology*, 35, 67–89,  
812 <https://doi.org/10.1175/JTECH-D-17-0081.1>, 2018.
- 813 Purser, R. J., Wu, W.-S., Parrish, D. F., and Roberts, N. M.: Numerical Aspects of the Application  
814 of Recursive Filters to Variational Statistical Analysis. Part I: Spatially Homogeneous and  
815 Isotropic Gaussian Covariances, *Monthly Weather Review*, 131, 1524–1535,  
816 [https://doi.org/10.1175/1520-0493\(2003\)131<1524:NAOTAO>2.0.CO;2](https://doi.org/10.1175/1520-0493(2003)131<1524:NAOTAO>2.0.CO;2), 2003.
- 817 Sheng, J., Zheng, Y., and Shen, X.: Climatology and environmental conditions of two types of  
818 quasi-linear convective systems with extremely intense weather in North China, *Acta*  
819 *Meteorologica Sinica*, 78(6), 877–898, 2020.
- 820 Shu-yuan, L., Yongguang, Z., and Zuyu, T.: The analysis of the relationship between pulse of LLJ  
821 and heavy rain using wind profiler data, *Journal of tropical meteorology*, 2003.
- 822 Skamarock, W., Klemp, J., Dudhia, J., Gill, D., Barker, D., Wang, W., Huang, X.-Y., and Duda, M.:  
823 A Description of the Advanced Research WRF Version 3, UCAR/NCAR,  
824 <https://doi.org/10.5065/D68S4MVH>, 2008.
- 825 St-James, J. S. and Laroche, S.: Assimilation of Wind Profiler Data in the Canadian  
826 Meteorological Centre’s Analysis Systems, *Journal of Atmospheric and Oceanic Technology*, 22,  
827 1181–1194, <https://doi.org/10.1175/JTECH1765.1>, 2005.
- 828 Wang, C., Chen, Y., Chen, M., and Shen, J.: Data assimilation of a dense wind profiler network  
829 and its impact on convective forecasting, *Atmospheric Research*, 238, 104880,  
830 <https://doi.org/10.1016/j.atmosres.2020.104880>, 2020.
- 831 Wang, C., Chen, M., and Chen, Y.: Impact of Combined Assimilation of Wind Profiler and  
832 Doppler Radar Data on a Convective-Scale Cycling Forecasting System, *Monthly Weather Review*,



- 833 150, 431–450, <https://doi.org/10.1175/MWR-D-20-0383.1>, 2022.
- 834 Wang, C., Chen, Y., Chen, M., and Huang, X.-Y.: Evaluation of two observation operator schemes  
835 for wind profiler radar data assimilation and its impacts on short-term forecasting, *Atmospheric*  
836 *Research*, 283, 106549, <https://doi.org/10.1016/j.atmosres.2022.106549>, 2023a.
- 837 Wang, S., Guo, J., Xian, T., Li, N., Meng, D., Li, H., and Cheng, W.: Investigation of low-level  
838 supergeostrophic wind and Ekman spiral as observed by a radar wind profiler in Beijing, *Front.*  
839 *Environ. Sci.*, 11, 1195750, <https://doi.org/10.3389/fenvs.2023.1195750>, 2023b.
- 840 Wang, Y., Gao, J., Skinner, P. S., Knopfmeier, K., Jones, T., Creager, G., Heiselman, P. L., and  
841 Wicker, L. J.: Test of a Weather-Adaptive Dual-Resolution Hybrid Warn-on-Forecast Analysis and  
842 Forecast System for Several Severe Weather Events, *Weather and Forecasting*, 34, 1807–1827,  
843 <https://doi.org/10.1175/WAF-D-19-0071.1>, 2019.
- 844 Zhang, L. and Pu, Z.: An Observing System Simulation Experiment (OSSE) to Assess the Impact  
845 of Doppler Wind Lidar (DWL) Measurements on the Numerical Simulation of a Tropical Cyclone,  
846 *Advances in Meteorology*, 2010, 743863, <https://doi.org/10.1155/2010/743863>, 2010.
- 847 Zhang, X., Luo, Y., Wan, Q., Ding, W., and Sun, J.: Impact of Assimilating Wind Profiling Radar  
848 Observations on Convection-Permitting Quantitative Precipitation Forecasts during SCMREX,  
849 *Weather and Forecasting*, 31, 1271–1292, <https://doi.org/10.1175/WAF-D-15-0156.1>, 2016.
- 850 Zhang, Y., Chen, M., and Zhong, J.: A Quality Control Method for Wind Profiler Observations  
851 toward Assimilation Applications, *Journal of Atmospheric and Oceanic Technology*, 34, 1591–  
852 1606, <https://doi.org/10.1175/JTECH-D-16-0161.1>, 2017.
- 853 Zhao, J., Gao, J., Jones, T. A., and Hu, J.: Impact of Assimilating High-Resolution Atmospheric  
854 Motion Vectors on Convective Scale Short-Term Forecasts: 1. Observing System Simulation  
855 Experiment (OSSE), *Journal of Advances in Modeling Earth Systems*, 13, e2021MS002484,  
856 <https://doi.org/10.1029/2021MS002484>, 2021a.
- 857 Zhao, J., Gao, J., Jones, T. A., and Hu, J.: Impact of Assimilating High-Resolution Atmospheric  
858 Motion Vectors on Convective Scale Short-Term Forecasts: 2. Assimilation Experiments of  
859 GOES-16 Satellite Derived Winds, *Journal of Advances in Modeling Earth Systems*, 13,  
860 e2021MS002486, <https://doi.org/10.1029/2021MS002486>, 2021b.
- 861 Zhao, J., Gao, J., Jones, T., and Hu, J.: Impact of Assimilating High-Resolution Atmospheric  
862 Motion Vectors on Convective Scale Short-Term Forecasts: 3. Experiments With Radar  
863 Reflectivity and Radial Velocity, *Journal of Advances in Modeling Earth Systems*, 14,  
864 e2022MS003246, <https://doi.org/10.1029/2022MS003246>, 2022.
- 865 Zhao, N., Yue, T., Li, H., Zhang, L., Yin, X., and Liu, Y.: Spatio-temporal changes in precipitation  
866 over Beijing-Tianjin-Hebei region, China, *Atmospheric Research*, 202, 156–168,  
867 <https://doi.org/10.1016/j.atmosres.2017.11.029>, 2018.
- 868 Zhong, S., Fast, J. D., and Bian, X.: A Case Study of the Great Plains Low-Level Jet Using Wind



- 869 Profiler Network Data and a High-Resolution Mesoscale Model, *Monthly Weather Review*, 124,  
870 785–806, [https://doi.org/10.1175/1520-0493\(1996\)124<0785:ACSOTG>2.0.CO;2](https://doi.org/10.1175/1520-0493(1996)124<0785:ACSOTG>2.0.CO;2), 1996.
- 871 Zhou, S., Yang, J., Wang, W., Gong, D., Shi, P., and Gao, M.: Shift of daily rainfall peaks over the  
872 Beijing–Tianjin–Hebei region: An indication of pollutant effects?, *Intl Journal of Climatology*, 38,  
873 5010–5019, <https://doi.org/10.1002/joc.5700>, 2018.
- 874 Zhuang, Z., Yussouf, N., and Gao, J.: Analyses and forecasts of a tornadic supercell outbreak using  
875 a 3DVAR system ensemble, *Advances in Atmospheric Sciences*, 33, 544–558,  
876 <https://doi.org/10.1007/s00376-015-5072-0>, 2016.
- 877 Ziegler, C. L.: Retrieval of Thermal and Microphysical Variables in Observed Convective Storms.  
878 Part 1: Model Development and Preliminary Testing, *Journal of Atmospheric Sciences*, 42, 1487–  
879 1509, [https://doi.org/10.1175/1520-0469\(1985\)042<1487:ROTAMV>2.0.CO;2](https://doi.org/10.1175/1520-0469(1985)042<1487:ROTAMV>2.0.CO;2), 1985.
- 880